1993ApJS...86..517Y

THE ASTROPHYSICAL JOURNAL SUPPLEMENT SERIES, 86:517–540, 1993 June

CIRCUMSTELLAR SHELLS RESOLVED IN THE *IRAS* SURVEY DATA. I. DATA PROCESSING PROCEDURE, RESULTS, AND CONFIDENCE TESTS

K. YOUNG,[1] T. G. PHILLIPS,[1] AND G. R. KNAPP[2]
Received 1992 February 19; accepted 1992 November 11

ABSTRACT

We have examined the *IRAS* 60 and 100 μm survey data covering 512 evolved stars and young planetary nebulae for evidence of spatially resolved structure. A simple model, consisting of a central unresolved source surrounded by a resolved isothermal shell, was fitted to the data for each star. Seventy-six stars were found to be resolved in the 60 μm data. Tests have been performed to verify that the extended structure seen is not an artifact of the data-processing algorithm.

Subject headings: circumstellar matter — infrared: stars — planetary nebulae: general — stars: late-type — stars: mass loss

1. INTRODUCTION

Shortly after the completion of the *IRAS* mission, it was realized that some highly evolved stars were surrounded by dusty envelopes large enough to have been clearly resolved by the satellite's 1′ resolution at 60 μm (Gillet et al. 1986; Hawkins 1990). Previous work on these objects has usually concentrated on producing high-quality maps of this extended structure. Because producing maps near the diffraction limit from *IRAS* data is difficult, only a small number have appeared in the literature. Our goal in this investigation was to conduct a more complete survey of the extended emission surrounding stars in the solar vicinity. We first examined all evolved stars which had been detected in a rotational transition of CO. Then, an additional list of stars not detected in CO was compiled, using *IRAS* color criteria, and examined in the same way.

The primary goal of the *IRAS* project was to survey the entire sky at 4 infrared wavelengths. While some specific objects were studied individually by the satellite, most of the sky was only observed as part of the all-sky survey. The overriding consideration in the design of the survey was to ensure the reliability of the derived data products; the Point Source Catalog, the Small-Scale Structure Catalog (hereafter SSSC), the Atlas of Low-Resolution Spectra (Olnon et al. 1986) and the maps of total sky brightness. A major difficulty in ensuring the integrity of these products was that the unprocessed survey data is contaminated with "detections" caused by cosmic rays, Earth-orbiting debris, and minor denizens of the solar system. In order to recognize and reject these spurious detections, the survey was designed to observe each position in the sky several times. For this reason, the *IRAS* survey data for a particular object consists of one or more sets of detector scans passing near the object's position.

Because the *IRAS* survey was designed to produce reliable measurements new objects, rather than to carry out detailed studies of well-known objects, there are several characteristics of the survey data which make it difficult to produce high-resolution images from the scans. The individual *IRAS* detectors were larger than the telescope's diffraction pattern, particularly in the direction parallel to the satellite's rotation axis (the "cross-scan" direction). Only by analyzing the data from several detectors, whose paths on the sky partially overlap, can information about source structure on spatial scales near the instrument's diffraction limit be recovered. Also, the detectors' outputs were passed through low-pass filters with cutoff frequencies well below the frequencies required for Nyquist sampling when the satellite was scanning the sky at the survey rate.

Several earlier investigations of the spatial information contained in the *IRAS* data have been published. Bauer & Stencel (1992) measured the widths of the individual 60 μm scans of nine nearby Mira variables, at 10% of maximum intensity. All of these stars also appear in our list of candidate objects and, with one exception (IRC +10°216), we are in agreement regarding which stars were and were not resolved. Stencel, Pesce, & Bauer (1988, 1989) summed all the 60 μm scans passing near 111 stars and measured the width of each star's composite profile at 10% and 5% of maximum, to search for extended emission. They found that one-fourth of their objects were resolved. Because Stencel et al. focused exclusively on supergiant stars of spectral types F0–M5, very few of the stars they examined appear in our list objects. Hawkins (1989, 1990) published fully deconvolved maps of several AGB stars, most of which also appear in our list.

Instead of deconvolving the *IRAS* data and producing a map, we fitted a model of a point source surrounded by dust to the data. There were two reasons for doing this. First, the sky coverage of *IRAS* data is nonuniform. If the star is very near one of the ecliptic poles, the survey data usually contains scans approaching the star from several different position angles. For these sources the effective point spread function for the survey is nearly circular (Moshir et al. 1989), and it should be possible to construct a map of the circumstellar material. More commonly, the survey data consists of several sets of scans, all approaching the star with very nearly identical position angles. This fact, combined with the saturation which may occur as soon as the star's image falls upon the detector, makes it difficult to construct a two-dimensional map of the material surrounding the star. On the other hand, since the detectors are

---

[1] California Institute of Technology, Pasadena, CA 91125.
[2] Department of Astrophysical Sciences, Princeton University, Princeton, NJ 08544.

extended in the cross scan direction, and since the distance of closest approach of each detector to the star's position varies, some two-dimensional information is contained in the survey data even if each detector approaches with the same position angle. The second reason for fitting a model, rather than producing an image, is that this approach directly gives values for the physically important parameters, such as the size and intensity of the dust shell's emission.

The data were fitted to a model consisting of an ellipsoidal envelope, at a single temperature throughout, with an unresolved point source at its center. Two of the axes of the ellipse were constrained to be perpendicular to the line of sight, and the semiminor axis was forced to be equal in length to the third axis, which lies along the line of sight. The emission is proportional to the column density of the dust, and the density of the dust is assumed to decrease linearly with the square of the distance from the star, but at differing rates along the different axes of the ellipsoid. The intensity of emission from the dust alone at position (x, y) is

$$I(x, y) = \frac{C}{\sqrt{k^2x^2 + y^2}} \arctan\left(\sqrt{\frac{b^2 - k^2x^2 - y^2}{k^2x^2 + y^2}}\right)$$

where x is the distance from the model center along the semimajor axis, y is the distance from the model center along the semiminor axis, C is a constant proportional to the rate of mass loss in dust (a model parameter), k is the ratio of the minor axis length to the major axis length (a model parameter), and b is the semiminor axis length (a model parameter). Since the formula above gives an infinite result at (0,0), the model assumes that the emission from dust reaches a constant value along lines of sight intersecting some inner radius where either the envelope is terminated, or the dust becomes optically thick. This inner radius is another parameter fitted by the model-fitting program (MFP).

In addition to the parameters C, k, and b of the dust model above, the model includes the intensity of the star, the right ascension and declination offsets of the model from the position given to ADDSCAN (an IPAC program which originally extracted the data), and a position angle in the sky of the major axis of the envelope, as parameters to be determined.

The model is fitted by minimizing the function

$$\text{Error} = \sum_{i=1}^{N_D} \sum_{j=1}^{N_{S_i}} \sum_{k=1}^{N_{P_{ij}}} \left| \frac{y_{ijk} - y_{ijk}(\boldsymbol{a})}{\sigma_i} \right|$$

where N_D is the number of *IRAS* detectors for a particular band, N_{S_i} is the number of scans for this source from detector i, $N_{P_{ij}}$ is the number of points in the jth scan of the ith detector, y_{ijk} is the kth data point from the jth scan of the ith detector, σ_i is the noise level of the ith detector relative to other detectors, $\boldsymbol{a}$ is a vector composed of the eight model parameters, and $y_{ijk}(\boldsymbol{a})$ is a two-dimensional integral of the model intensity at the sky position corresponding to y_{ijk} multiplied by the response function for the ith detector,

$$y_{ijk}(\boldsymbol{a}) = \int_{-S_i}^{S_i} \int_{-T_i}^{T_i} I(\boldsymbol{a}, s, t) R_i(s, t) ds dt .$$

The limits in the integral above correspond to the spatial extent of the ith detector, which for the 60 μm detectors is ±3'.0 in the in-scan direction and ±3'.3 in the cross-scan direction. $R_i(s, t)$, the two-dimensional response function of the ith detector, is calculated from the Moshir response functions (Moshir 1989). These response functions were derived from a set of 32 Additional Observations (AOs) of the planetary nebula NGC 6543. The functions do not perfectly represent the point spread function of the *IRAS* detectors during survey observations, for two reasons. The first reason is that NGC 6543 was slightly resolved by *IRAS*. The second reason is that when the AO data were taken, the satellite scanned the sky more slowly than it did during survey observations. Since the detector outputs were passed through low-pass filters, and since the detectors themselves were hysteretic, the response functions derived from AOs are less extended on the sky than a point source observed at the survey scan rate would be. Since the first problem makes the templates too large on the sky, and the second makes them too small, the problems cancel each other to some extent. Tests, described below, were performed to judge how well the Moshir functions mimicked the shape of a point source observed during the survey. We calculated $y_{ijk}(\boldsymbol{a})$ by Simpson's rule integration. The function *error* was minimized in the eight dimensional space of model parameters by a direction set algorithm (Press 1986). The integrals were calculated to a precision of 5%, and the direction set algorithm was iterated until an iteration passed during which none of the model parameters changed by as much as 5%.

The absolute value of the deviation of the model from the data was minimized, rather than the square of the deviation, which is a more common figure of merit. This approach was taken because the noise in *IRAS* data is very non-Gaussian. Radiation hits and emission from dust near the satellite produced frequent spikes in the data, which have a noticable effect on the MFP if the square of the deviation is used as the figure of merit.

2. DATA-PROCESSING STEPS

Of the four *IRAS* bands, dust emission is visible primarily in the 60 and 100 μm data, where the emission from the central star is less dominant. The 60 μm data were analysed first, because the 60 μm data yield higher resolution and are much less effected by infrared cirrus emission. Each star's data set was produced by the default ADDSCAN processing and consists of all scans in which the star passes within 1'.7 of the detector center.

The first step in processing the data was to subtract a linear baseline from the Calibrated Raw Detector Data (CRDD). The baseline is fitted to two windows 15' away from the star's position. If one of the windows contained emission from another source, then the windows were moved further from the source to regions showing no emission. Obvious noise spikes were also removed at this point.

The first pass of the MFP tried to fit just three of the model's eight parameters: the point source intensity, and the right ascension and declination offsets. After these three parameters were been determined, the MFP minimized the *error* function with respect to six parameters: point source intensity, dust shell density, radius at which dust becomes optically thick, semimajor axis length, aspect ratio, and position angle. The point source intensity had to be redetermined in this second fitting loop, because the first loop might have overestimated the intensity of the point source by ignoring the contribution from the resolved region. If MFP reported that the CSS extended as far as 15′ from the star, the baseline windows were moved further from the central position and the data were reprocessed. Figure 1 compares the results of the two passes of the MFP to the CRDD data, for the case of the carbon star Y CVn.

For those objects which the MFP indicated were extended, the MFP was run a second time. For this run a larger data set was used, consisting of all scans which passed within 10′ of the star's position. Figure 2 shows the increased coverage afforded by this larger data set, again for Y CVn. In the case of Y CVn, as with most of the stars, all the scans approached the star from nearly the same position angle. As a result of this, the extent of the dust in the direction perpendicular to the scans (the cross-scan direction) was very poorly constrained by the small data set. The larger data set allowed the size of the shell in the cross-scan direction to be determined much more accurately. This second 60 μm processing pass was not performed for the four brightest resolved sources: CIT 6, α Ori, *o* Cet, and IRC +10°216. The CRDD data for these four objects shows optical cross talk caused by the telescope's secondary support spider. None of these objects showed optical cross talk in the 100 μm band, except IRC +10°216 which showed it only weakly.

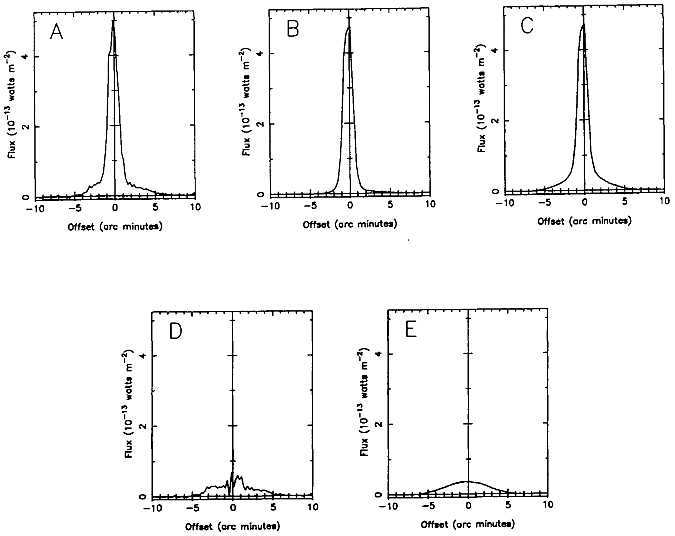

FIG. 1.—(*a*) All the scans for the source Y CVn, averaged together. To produce this plot the data points were averaged in bins 15″ wide. The bin in which to place a data point was determined by the distance of the point from the source, in the in-scan direction. (*b*) Results from the first pass of the model fitting program (MFP) are shown. Synthetic data were produced by calculating the flux predicted by the model for each point at which a measurement was taken. The model used in this plot consisted of the MFP's best fit for the first three parameters: point source intensity, and right ascension and declination offsets. (*c*) The results of the second pass of the MFP are shown. Synthetic data were produced, using the MFP's final best fit for both the point source and dust shell. (*d*) This plot shows the residual flux remaining after the best-fit point source is subtracted from the data. Some residual flux remains, from a resolved dust shell. (*e*) The rightmost plot shows synthetic data for the dust shell only.

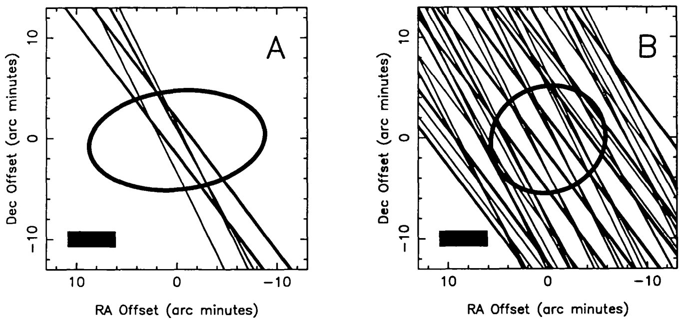

FIG. 2.—(*a*) The coverage of the source Y CVn, using the default ADDSCAN selection criteria which selects all scans passing within 1′.7 of the source. Each line represents the path on the sky of an *IRAS* detector, and some lines overlap. The ellipse plotted is the size and shape of the CSS, determined from these 10 scans. Since all the passes approached the source from nearly the same angle, the size of the dust shell in the orthogonal direction is poorly constrained. (*b*) The increased coverage when all 56 scans which passed within 10′ are used, along with the shape of the CSS derived from those scans. Even though all scans still approach from about the same angle, the size of the dust shell is now well constrained in all directions, and the CSS is seen to be nearly circular. In both figures, the black box shows the size of the largest *IRAS* 60 μm detector.

3. RESULTS

The initial list of objects processed consisted of all the evolved stars for which a detection of emission in a rotational line of CO had appeared in the literature (by 1989). Four of these stars fell within the small areas of the sky not covered by the *IRAS* survey. Sixty-six of these stars were either near other sources or imbedded in regions of extended emission, resulting in badly curved baselines. These stars were rejected. The data for the remaining 213 stars were processed by the MFP. The calculations consumed more than 1 CPU year on a VAX 11/750 computer. 152 of these stars did not appear to be extended. Five of the stars which did appear extended had a CIRR2 value greater than 4 in the PSC, suggesting the region may have been contaminated by cirrus. These stars were also rejected.

The example of R CrB, which was very clearly resolved by *IRAS* (Gillet et al. 1986), yet has not been detected in CO, led us to look for additional stars which might have been resolved. In an effort to find other such objects, all objects listed in the PSC matching the following criteria were examined:

PSC CIRR2 flag < 5
and
(1) {[12 μm flux/25 μm flux) < 3.7 and
60 μm flux > 2.0 Jy and
all four PSC fluxes have quality flags > 1 and
spectral type, if available, later than K and
(an association in
the General Catalog of Variable Stars or
the General Catalog of Cool Carbon Stars or
the General Catalog of S Stars)]

or

[an association in the SSSC within 120″ and
a SSSC 60 μm or 100 μm flux > 0 and

1993ApJS...86..517Y

a SSSC Cir flag < 5 and
(12 μm flux/25 μm flux) < 4.0 and
spectral type, if available, later than K and
no extragalactic associations]}

or

(2) a Mira variable within 500 pc (using distance estimates from Jura & Kleinmann 1992 if available, otherwise using the Bowers & Hagen 1984 P-L-S relationship).

An additional 235 stars matched the above criteria. This group of objects will be referred to as the "Additional Objects." Of them, 116 had bad baselines, and 95 appeared to be unresolved.

Table 1 lists all the stars from the CO selected list that were rejected, along with those which were not found to be extended. Table 2 does the same for the Additional Objects.

Figures 3–15 show the results of the MFP for the 78 stars that appeared extended in the 60 μm data, and for IRC +10°216 which appeared extended, but badly saturated the detectors. Three plots are shown for each star. The first plot shows the average of all the survey scans passing within 1′ of the star's position. To produce this plot, the distance in the scan direction of the detector's center from the star's position was used to select the bin in which each data point would be averaged. There were four bins per arcminute. The second plot, labeled "data," shows these same averaged scans after the point source, fitted by the MFP, has been subtracted. The third plot, labeled "model," shows synthetic averaged data. This plot was constructed by calculating the predicted flux from the extended portion of the model, at every point where data were actually measured. A bar is plotted under both the "data" and "model" plots, the length of which is the "diameter" of the CSS, defined as the geometric mean of the shell's major and minor axes.

TABLE 1

STARS FROM THE CO LIST WHICH WERE EXAMINED AND REJECTED

Stars not observed during *IRAS* survey				
IRC−10236	NGC 7027	IRC+40483	IRC+00509	
Stars with curved baselines				
IRAS 00210+6221	OH 127.8 − 0.0	OH 141.7 + 3.5	U Ari	U Cam
RX Lep	IRC−10139	S Aur	S Ori	M 1 − 7
M 1 − 8	RY Mon	W CMa	IRC−20131	NGC 6072
RS Sco	RR Sco	IRAS 17217-3916	IRAS 17371-3021	OH 0.9 + 1.3
TW Oph	OH 11.4 + 6.6	NGC 6445	IRAS 17581-1744	VX Sgr
NGC 6563	M 4 − 9	CRL 2154	IRAS 18248-0839	IRAS 18269-1257
OH 17.7 − 2.0	OH 26.5 + 0.6	IRC+00365	IRAS 18424+0346	R Sct
OH 30.1 − 0.7	S Sct	OH 32.8 − 0.3	OH 39.7 + 1.5	IRC+10401
V Aql	R Aql	IRAS 19068+0544	OH 44.8 − 2.3	Vy2 − 2
RT Aql	IRAS 19477+2401	IRAS 20028+3910	IRAS 20435+3825	IRAS 20532+5554
IRAS 21003+4801	V1549 Cyg	IRAS 21147+5110	IRAS 21223+5114	IRAS 21282+5050
IC 5117	IRAS 21318+5631	IRC+40485	RU Cyg	IRAS 21449+4950
M 2 − 51	OH 104.9 + 2.5	CRL 2985	CRL2999	CRL 3011
IRC+60427				
Stars which were processed, but did not appear to be extended				
IRC+40004	T Cas	R And	IRC+10011	IRC+30021
IRC+60041	Z Psc	CRL 190	S Cas	W And
IRAS 02152+2822	R For	CRL 341	CIT 4	IRC−30023
R Hor	IRAS 03074-8732	TW Hor	CRL 482	OH 138.0 + 7.3
IRC+50096	CRL 5102	NML Tau	IRC+60144	CRL 618
IRAS 04530+4427	TX Cam	IRC+50137	NSV 1835	IRAS 05136+4712
IRC+60154	CRL 809	IRC+70066	Y Tau	IRC+40149
V Cam	CRL 865	TU Gem	CRL 933	CRL 935
CRL 954	IRC+60169	CRL 971	IRC−20101	GX Mon
CL Mon	R Vol	CRL 1085	IRAS 07134+1005	VY CMa
IRAS 07217-1246	S CMi	M 1 − 16	NGC 2440	OH 231.8 + 4.2
IRAS 07582-1933	IRAS 08045-1524	IRAS 08074-3615	CRL 1235	R Cnc
CRL 5250	W Cnc	CRL 5254	X Hya	IRAS 09371+1212
R LMi	IW Hya	X Vel	V Hya	IRAS 11308-1020
RU Vir	S Vir	CRL 4211	S CrB	IRAS 15194-5115
WX Ser	V CrB	R Ser	CRL 1822	RU Her
IRAS 16105-4205	U Her	g Her	M 2 − 9	CPD−56
CRL 1922	V463 Sco	NGC 6302	CRL 6815S	IRC+20326
MW Her	CRL 5379	HD 161796	89 Her	T Dra
FX Ser	CRL 2135	CRL 2155	T Lyr	CRL 2199
IRC+10365	X Oph	IRC+20370	IRC+10374	IRAS 18467-4802
CRL 2259	IRC−30398	RS Cra	V3880 Sgr	IRC−30404
CRL 2343	W Aql	CRL 2362	IRC−10502	IRC+10420
CRL 2417	M1 − 92	IRAS 19346+1209	IRAS 19454+2920	GY Aql
IRAS 19475+3119	IRAS 19500-1709	CRL 2477	RR Aql	CRL 2494
Z Cyg	IRC−10529	NSV 12961	IRC+80040	V Cyg
CRL 2646	IRAS 20541-6549	CRL 2686	CRL 2688	IRC+00499
UU Peg	CRL 5625S	IRAS 21373+4540	V460 Cyg	RT Cep
IRAS 21489+5301	IRAS 21554+6204	TW Peg	CRL 2901	IRAS 22272+5435
IRAS 22303+5950	CRL 3068	CRL 3099	IRAS 23268+6854	IRAS 23279+5336
IRC+40540	IRAS 23321+6545			
Stars which appeared to be extended, with a PSC CIRR2 flag > 4				
IRAS 05104+2055	RS Lib	χ Cyg	T Cep	μ Cep [A]

[A] Although it is located in a region contaminated by cirrus, it is likely that μ Cep is truly resolved in the *IRAS* data (Stencel et al. 1988; Hawkins 1989).

TABLE 2

STARS FROM THE ADDITIONAL OBJECTS LIST WHICH WERE EXAMINED AND REJECTED

Stars with curved baselines				
PK 118+02.1	VX And	CE And	TT Per	S Per
SS Cep	BE Cam	BR Eri	RS Eri	IR Per
BZ Tau	DV Tau	RT Ori	V883 Ori	S Col
TV Gem	CRL 5188	CR Gem	FX Mon	NP Pup
BM Gem	RX Cnc	Z Cnc	FK Hya	RV Hya
SZ Car	SAO 238059	IRAS 10308 − 6122	BI Car	IRAS 10501 − 5556
AF Leo	C 1882	S Crt	Z UMa	TZ Vir
BB Cru	TV Cen	AA Cru	SS Vir	V497 Cen
V744 Cen	WY Boo	AQ Cen	C 2147	UZ Cir
Y Cen	GI Lup	S Ser	R Cir	RV Tra
Z Sco	NSV 7459	SS Nor	C 2336	V594 Her
R UMi	AF Sco	AH Dra	V850 Oph	TU Sco
V617 Sco	V522 Oph	IRC−20360	C 2451	V492 Sco
TY Dra	RU Sco	BG Oph	V762 Sgr	V438 Sco
OP Her	AU Her	EK CrA	WY Her	IRC−10392
V1804 Sgr	V529 Her	V1014 Oph	IRC+10356	TW Lyr
SS Tel	V348 Sgr	AM CrA	V2059 Sgr	SU Sgr
RX Tel	V1256 Sgr	RY Sgr	YZ Dra	V859 Aql
DI Sgr	V464 Aql	RR Sgr	V468 Cyg	RX Sge
CRL 2492	V718 Cyg	GN Cyg	AE Cap	V372 Cyg
RS Del	AI Cyg	V570 Cyg	RX Vul	UX Cyg
RS Cap	PK 97+3.1	VV Cep	SS Peg	AB Aqr
DG Cep	RX Lac	BC And	SV Aqr	PZ Cas
RT Cas				
Stars which were processed, but did not appear to be extended				
SY Scl	S Scl	T Cet	T And	UY Cet
TU And	RW And	ST Psc	R Psc	SV Psc
UZ Cet	RY Cet	R Cet	R Tri	W Hor
T Ari	Z Eri	X Hor	RR Eri	U Hor
UU Eri	T Cam	R Cae	SY Men	T Lep
S Pic	U Dor	RT Lep	TW And	S Lep
CRL 915	U Lyn	X Gem	L2 Pup	SV Lyn
RZ UMa	FZ Hya	RT Hya	AK Hya	CRL 5252
EY Hya	RT Cnc	FF Hya	R UMa	ST UMa
C 1886	AZ UMa	T Crv	NSV 5868	U CVn
T Com	R CVn	AY Vir	RW CVn	RU Hya
U UMi	RS Vir	V Boo	RV Boo	Y Lib
S UMi	CRL 1788	BG Ser	RS CrB	AT Dra
RY CrB	TV Dra	U Tel	Nova Aql 1919	CH Cyg
V2234 Sgr	R Tel	RT Sgr	Y Tel	U Mic
TZ Aql	Y Aqr	U Del	W Aqr	S Ind
V Mic	R Gru	UU Tuc	DZ Aqr	S Gru
RV Peg	R Peg	Y Scl	S Peg	BU And
R Aqr	EY And	S Phe	Z Peg	W Cet

4. TESTS FOR RELIABILITY OF THE RESULTS

One can easily imagine problems that might cause the MFP to fit a spurious resolved component to the data. For example, if the satellite pointing reconstruction was poor for some proper subset of the scans covering a particular star, then the peak intensities for those scans would not appear to fall at the star's true position. If all the scans for the star were then summed via ADDSCAN, the star's detection profile would be artificially broadened. In order to verify that our results were not badly contaminated by such errors, several tests were performed to determine whether or not the extended emission reported by the MFP was real. The first test was to run the MFP using data for sources that should not be resolved. Figure 16 shows the results of running the MFP on the 60 μm data for six galaxies which were unresolved at all *IRAS* wavelengths (Soifer 1989). Except for the case of NGC 2966 (Fig. 17*c*), the data for each of these galaxies is well approximated by the point source that the MFP fitted. When the model point source is subtracted from the NGC 2966 data, the fit is seen to be quite poor at small offset values. This defect, which is also seen in many of the stellar cases, probably arises from small errors in the position reconstruction of individual survey scans. While the MFP fitted a position offset to the data set as a whole, no attempt was made to correct for position errors on a scan by scan basis. Because we were searching for extended structure, corresponding to low spatial frequencies in the data, small position errors could not greatly affect our results. This is confirmed by the fact that in none of the galaxy test cases, including NGC 2966, did the MFP fit a significant extended component.

Although the infrared cirrus emission was detected primarily at 100 μm, it occasionally was seen at 60 μm. If the area around the star being examined is contaminated by infrared cirrus emission, then the MFP might fit a dust shell to this emission even though it is not circumstellar in origin. A value greater than 4 for the PSC CIRR2 flag indicates the source is in a region which may be contaminated by cirrus emission. Figure 17*a* shows the CIRR2 flag distribution of all objects which the MFP reported were unresolved. The average CIRR2 value for this group is 3.5. Figure 17*b* shows the distribution for the objects which appeared to be resolved, including those with CIRR2 flags greater than 4. For this group, the average value is 2.7. On average, the objects which appear to be extended are in regions which are less apt to be contaminated with cirrus emission than are the unresolved objects, so it is unlikely that the

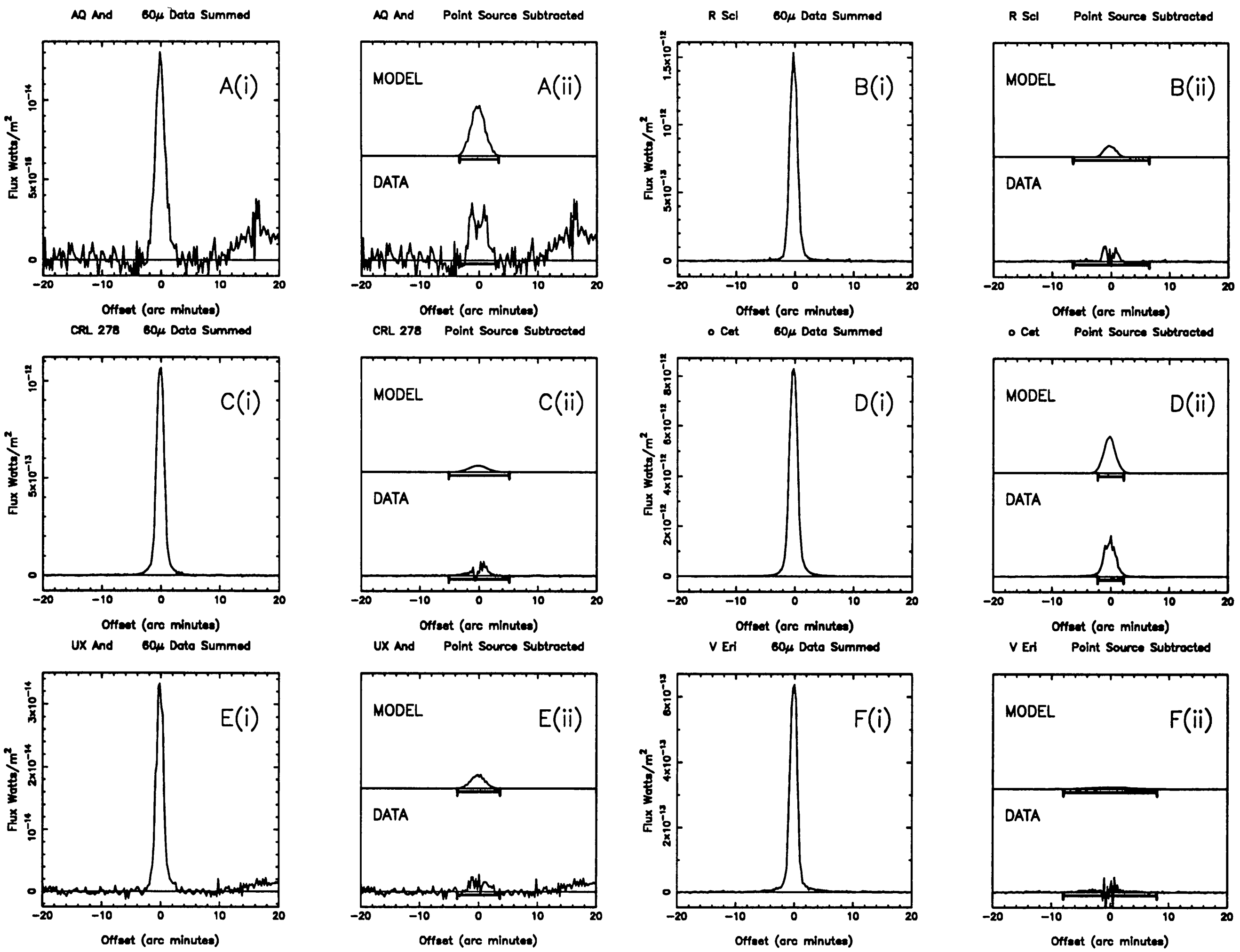

FIG. 3.—The results of the MFP are compared with the 60 μm CRDD data for six stars, AQ And, R Scl, CRL 278, *o* Cet, UX And, and V Eri. For each star, two plots are shown. In plots (i), the raw data have been summed into 0.'25 bins. The offset refers to the scan-direction component of the detector's distance from the star. In plots (ii), synthetic binned data, corresponding to the best-fit model for the extended emission, is compared with the binned CRDD data after the model's point source component has been subtracted. The vertical scale in plots (ii) is the same as in plots (i). The length of the bars shown in plots (ii) is equal to the shell's "diameter," defined here as the geometric mean of the shell's major and minor axes.

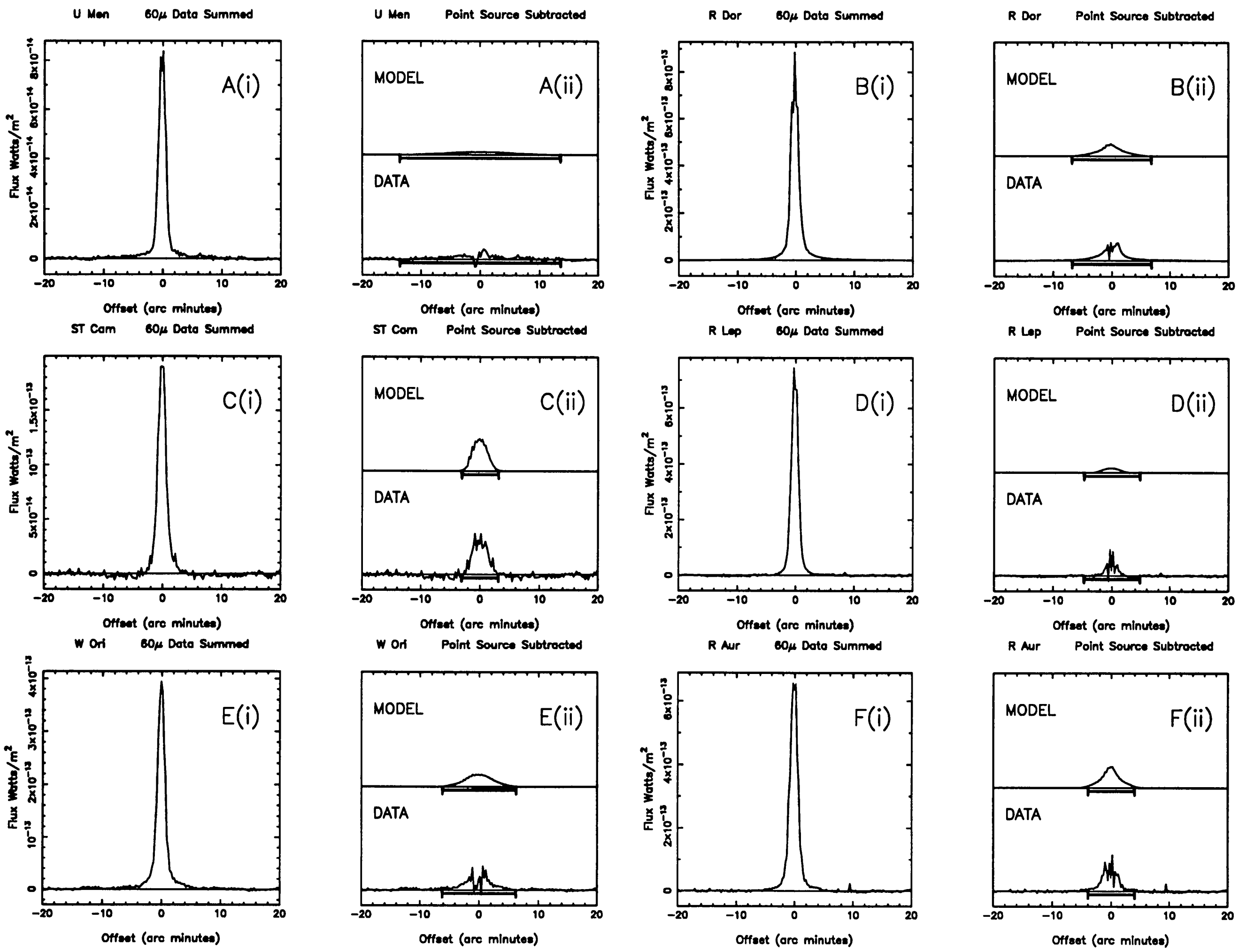

FIG. 4.—This figure shows plots of the same type as in Fig. 3, for the stars U Men, R Dor, ST Cam, R Lep, W Ori, and R Aur

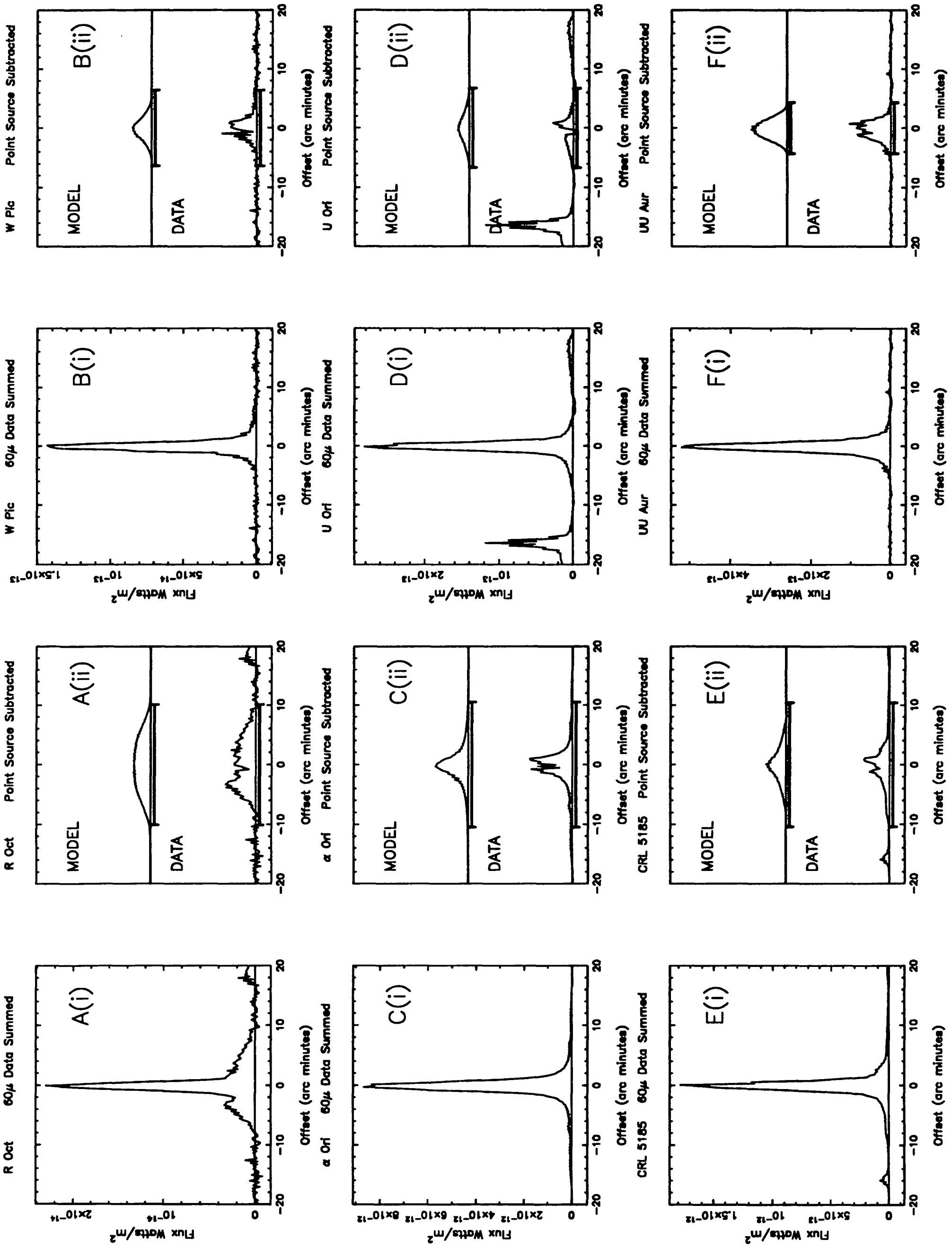

FIG. 5.—This figure shows plots of the same type as in Fig. 3, for the stars R Oct, W Pic, α Ori, U Ori, CRL 5185, and UU Aur

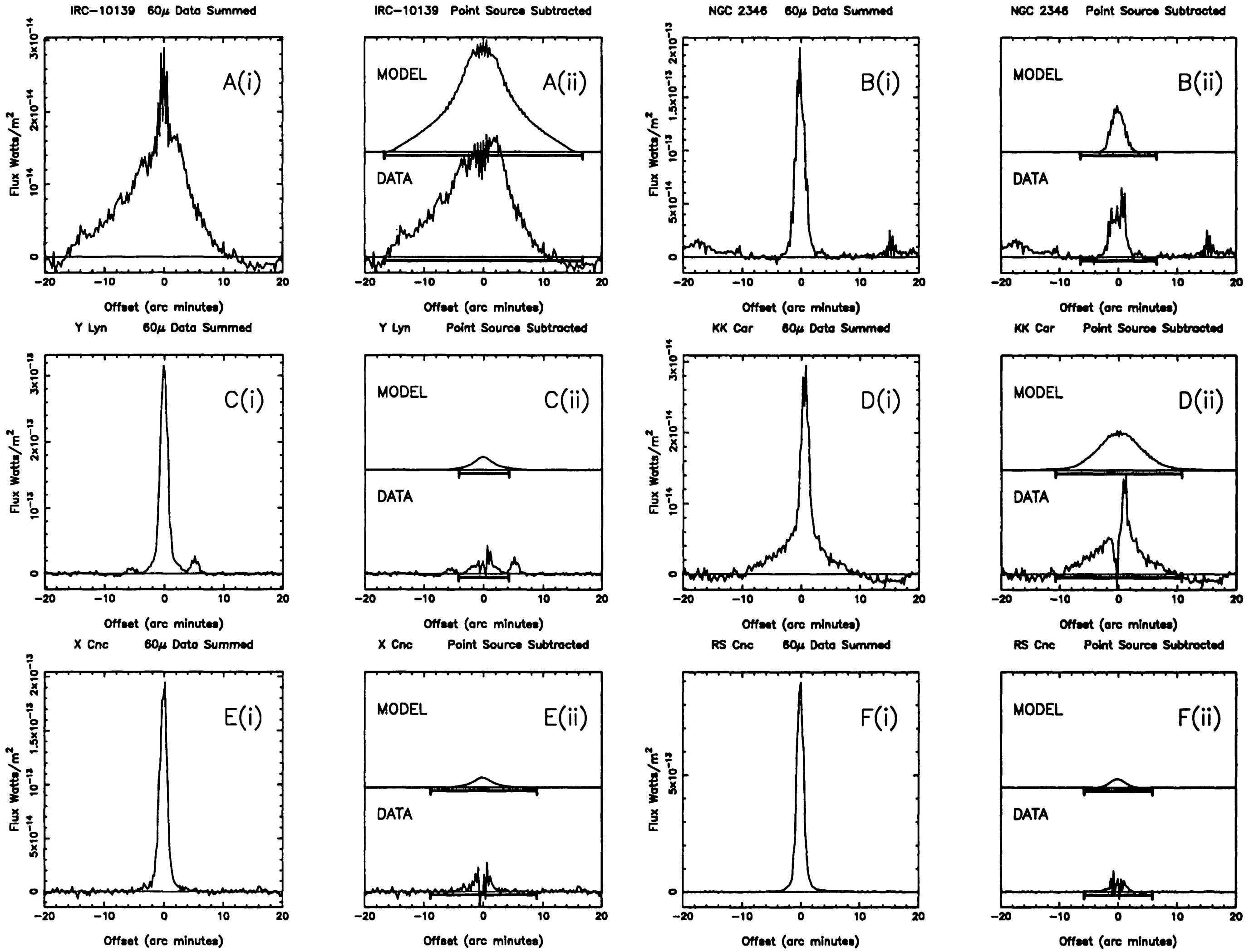

FIG. 6.—This figure shows plots of the same type as in Fig. 3, for the stars IRC −10139, NGC 2346, Y Lyn, KK Car, X Cnc, and RS Cnc

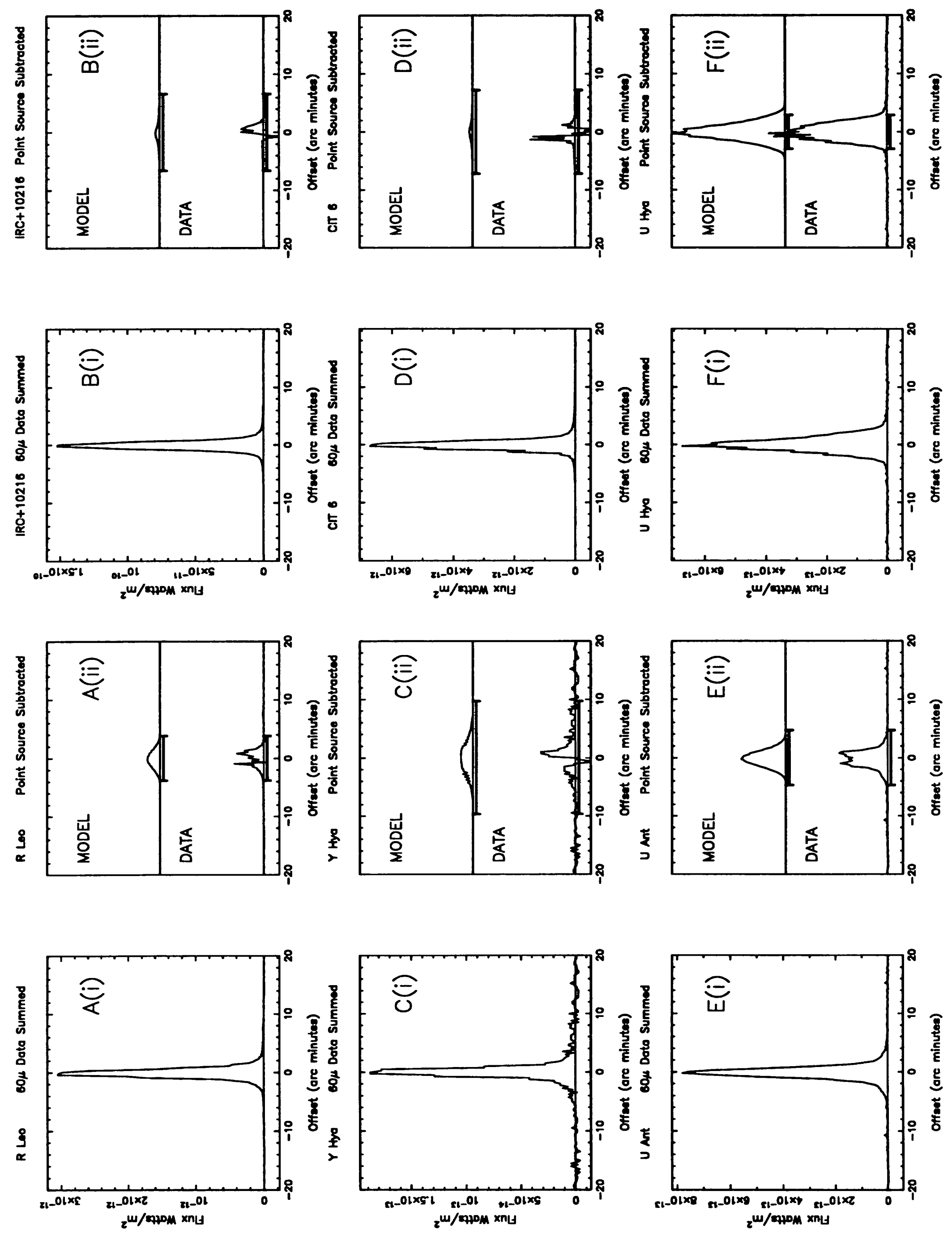

FIG. 7.—This figure shows plots of the same type as in Fig. 3, for the stars R Leo, IRC +10216, Y Hya, CIT 6, U Ant, and U Hya

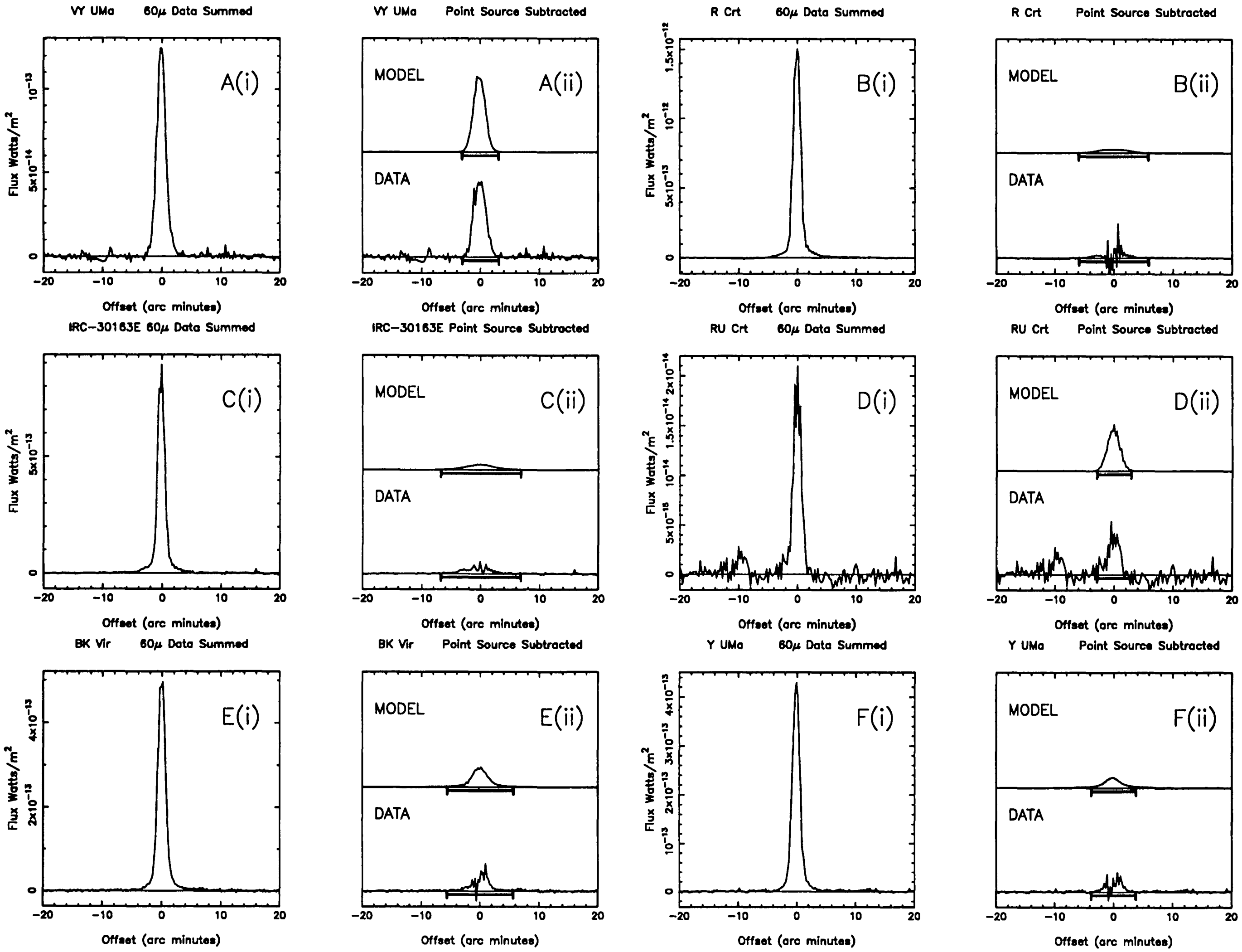

FIG. 8.—This figure shows plots of the same type as in Fig. 3, for the stars VY UMa, R Crt, IRC −30163E, RU Crt, BK Vir, and Y UMa

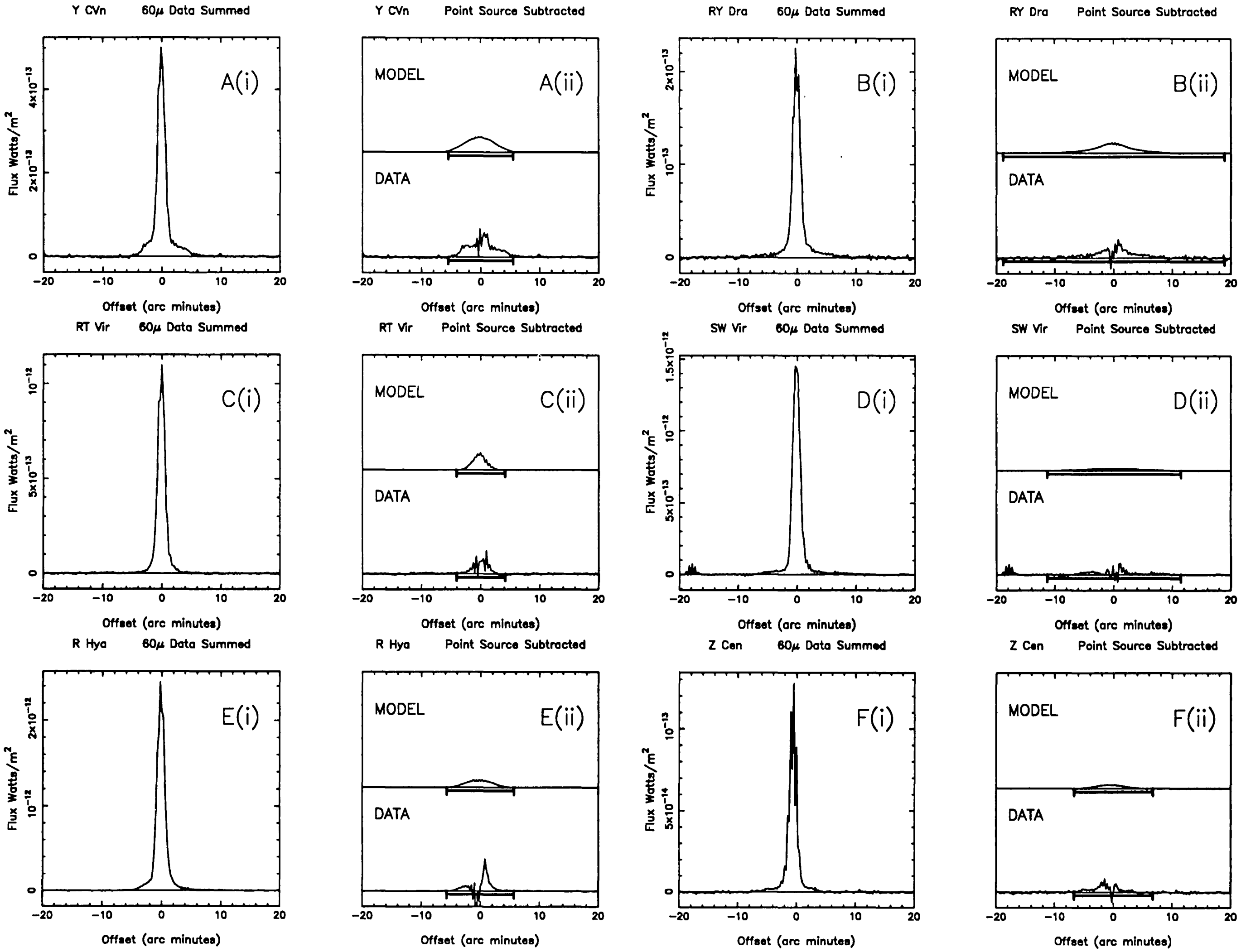

FIG. 9.—This figure shows plots of the same type as in Fig. 3, for the stars Y CVn, RY Dra, RT Vir, SW Vir, R Hya, and Z Cen

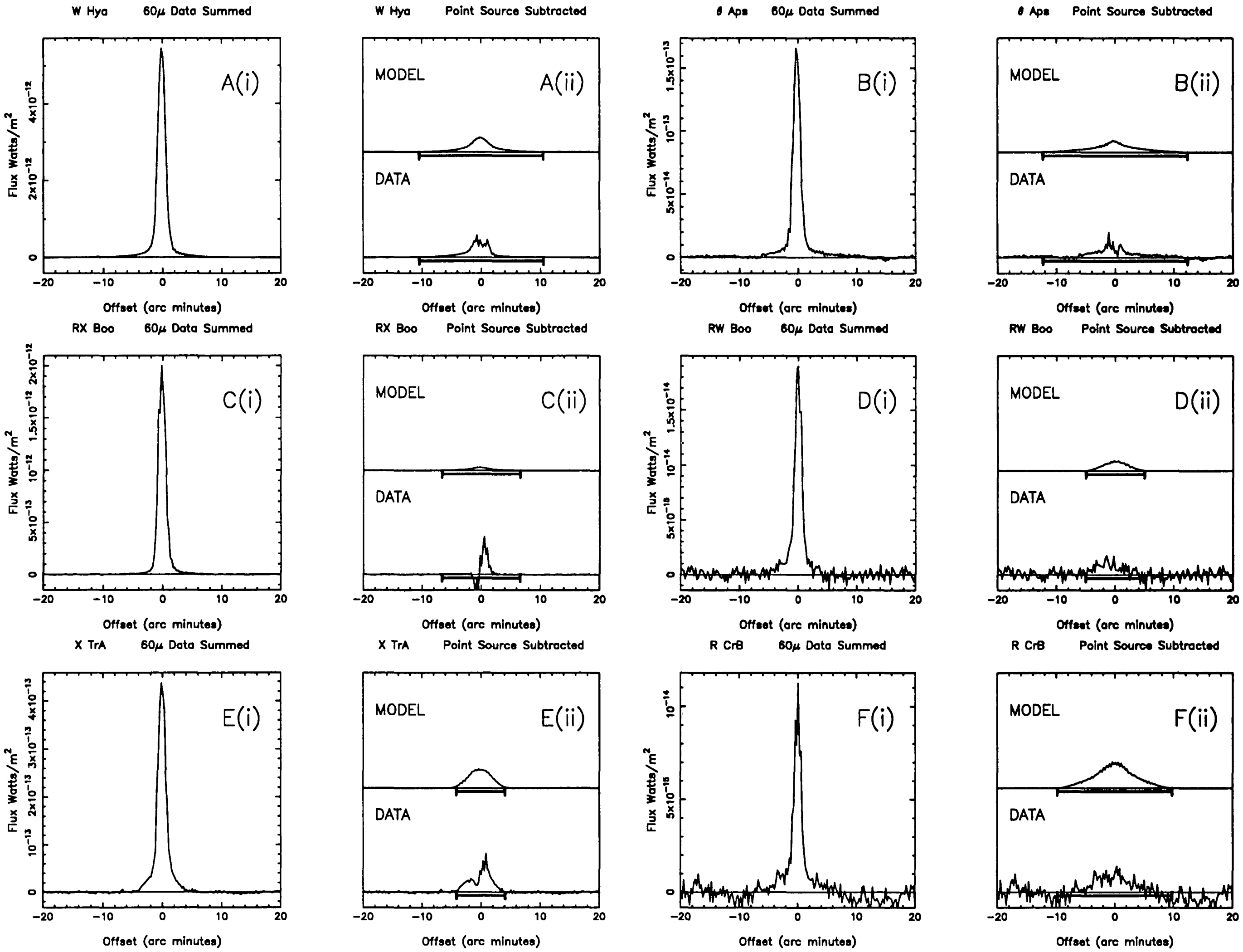

FIG. 10.—This figure shows plots of the same type as in Fig. 3, for the stars W Hya, θ Aps, RX Boo, RW Boo, X TrA, and R CrB

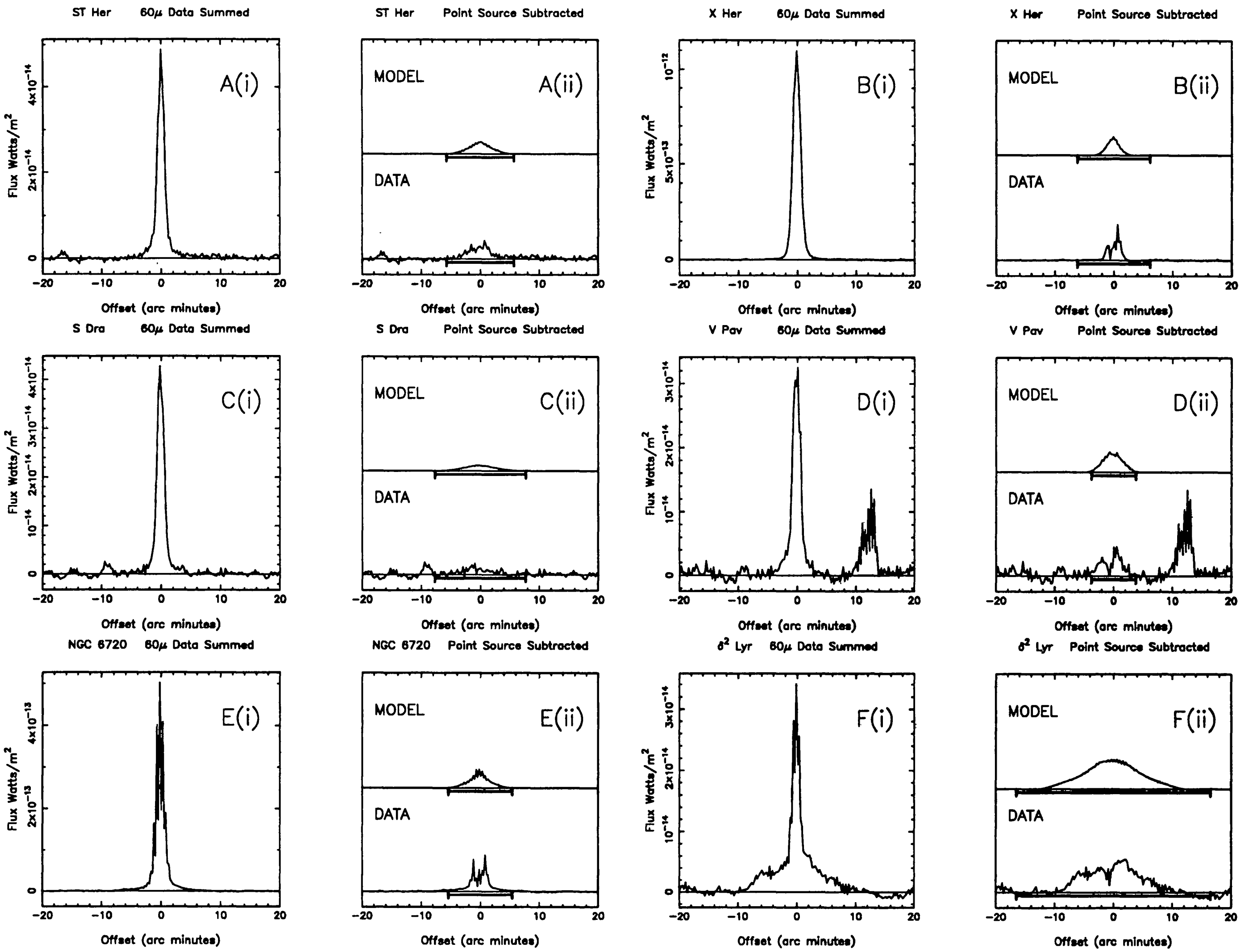

FIG. 11.—This figure shows plots of the same type as in Fig. 3, for the stars ST Her, X Her, S Dra, V Pav, NGC 6720, and δ^2 Lyr

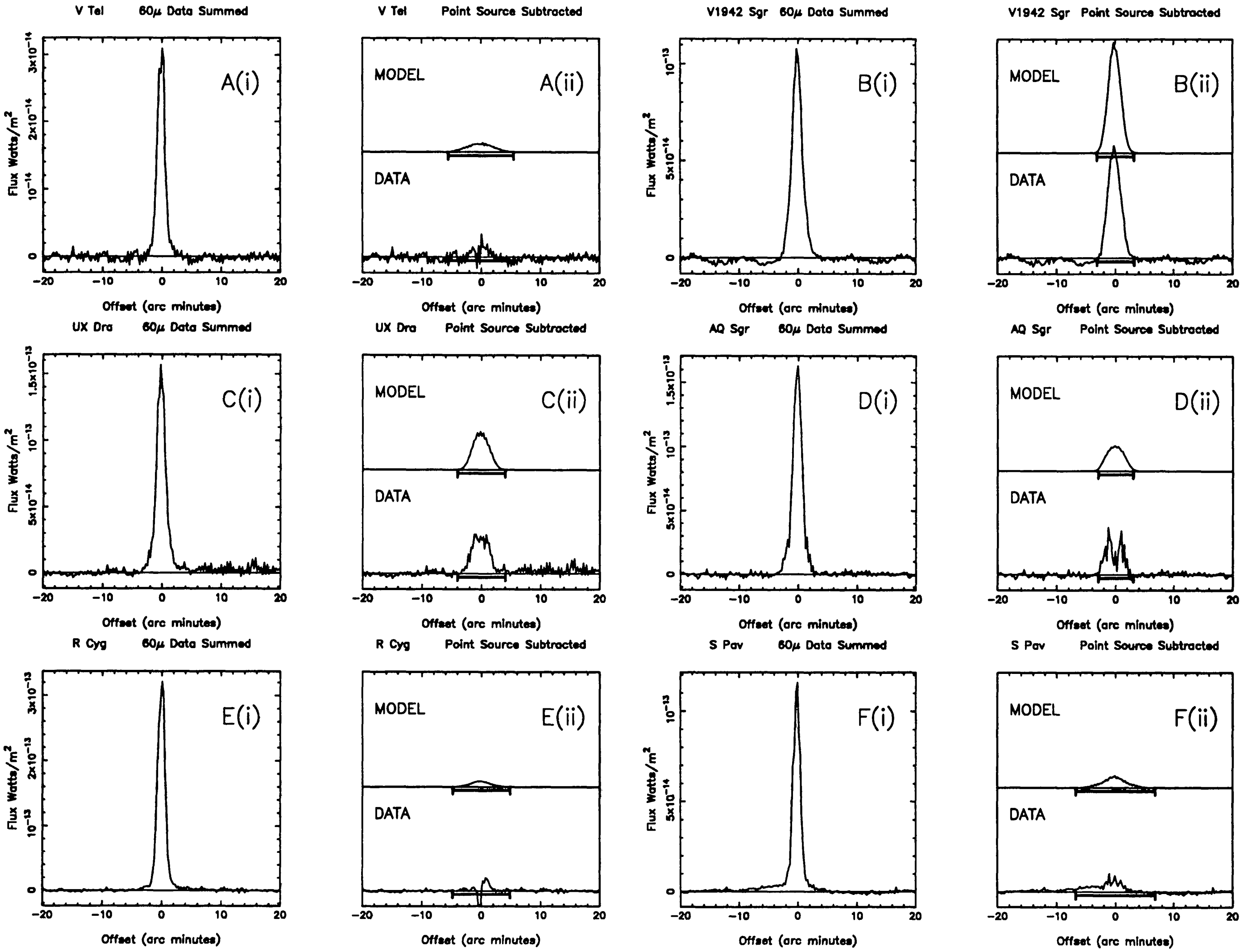

FIG. 12.—This figure shows plots of the same type as in Fig. 3, for the stars V Tel, V1942 Sgr, UX Dra, AQ Sgr, R Cyg, and S Pav

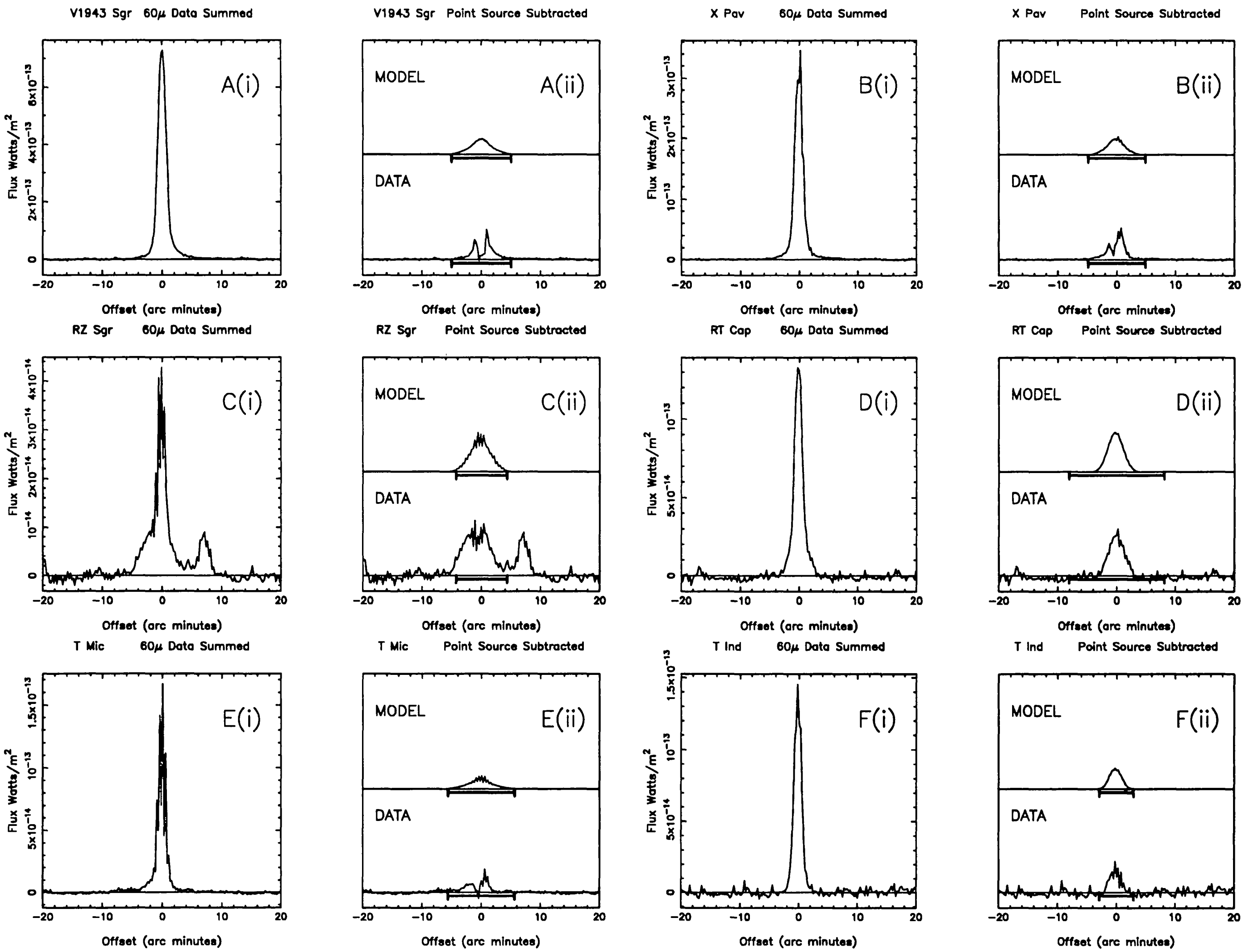

FIG. 13.—This figure shows plots of the same type as in Fig. 3, for the stars V1943 Sgr, X Pav, RZ Sgr, RT Cap, T Mic, and T Ind

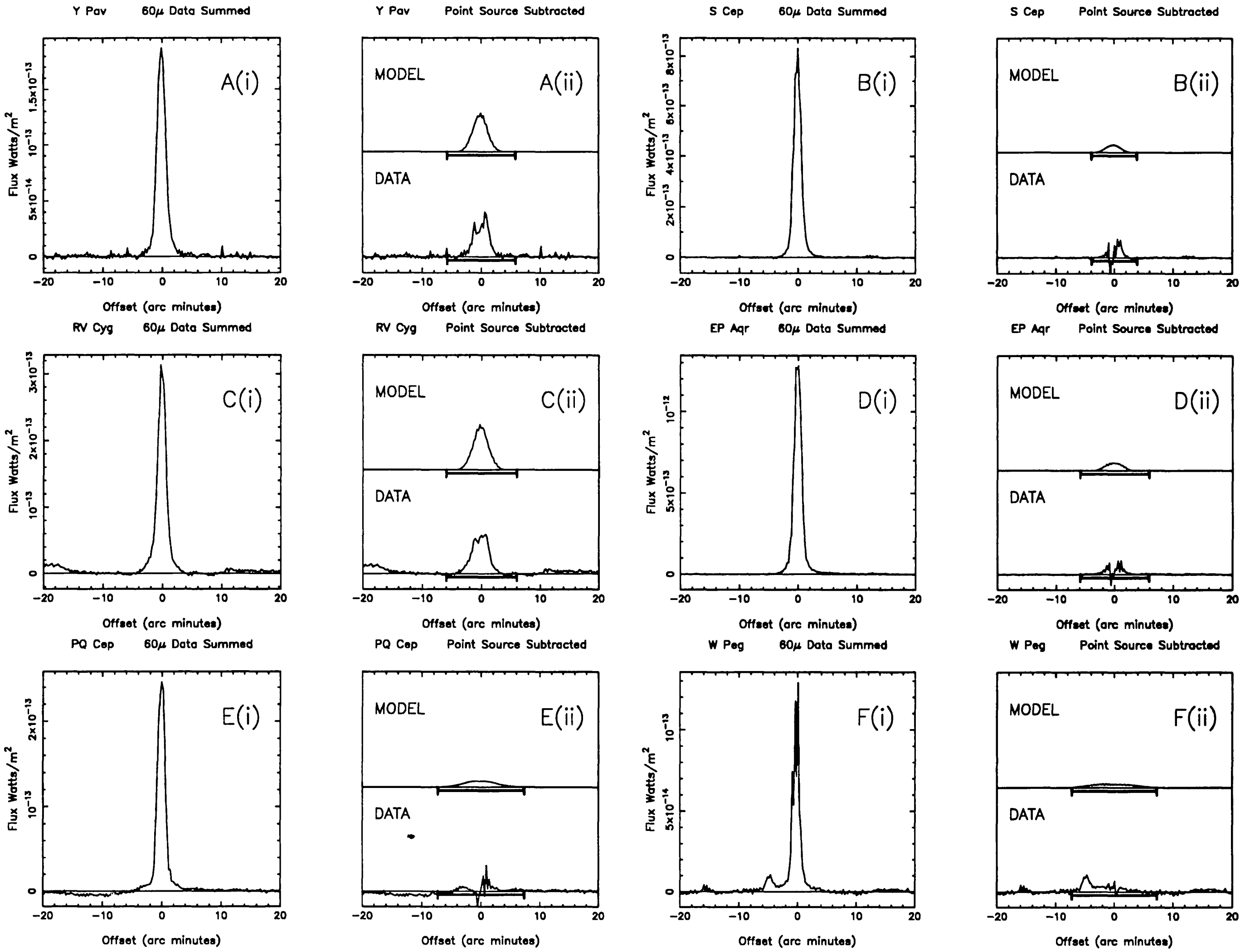

FIG. 14.—This figure shows plots of the same type as in Fig. 3, for the stars Y Pav, S Cep, RV Cyg, EP Aqr, PQ Cep, and W Peg

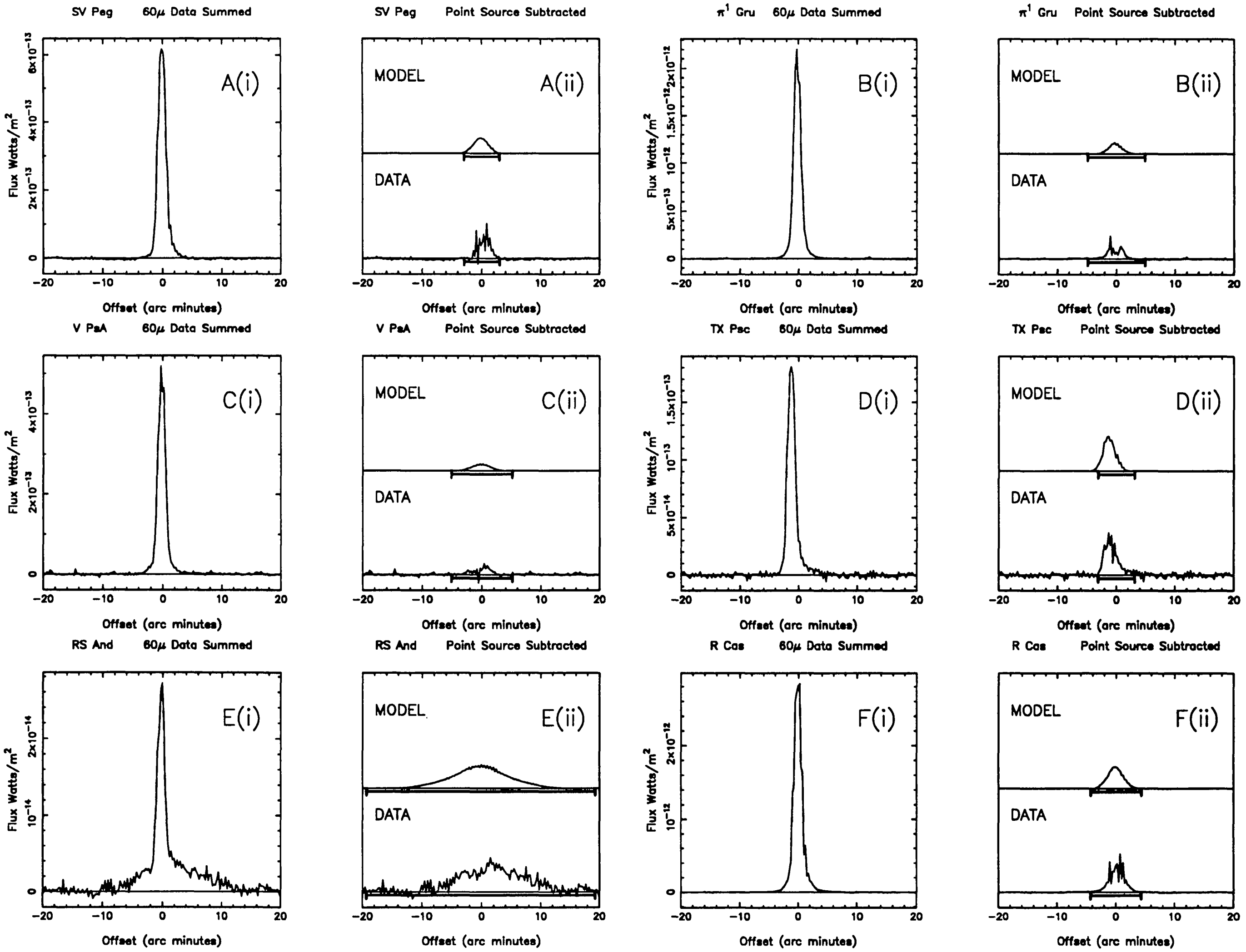

FIG. 15.—This figure shows plots of the same type as in Fig. 3, for the stars SV Peg, π^1 Gru, V PsA, TX Psc, RS And, and R Cas

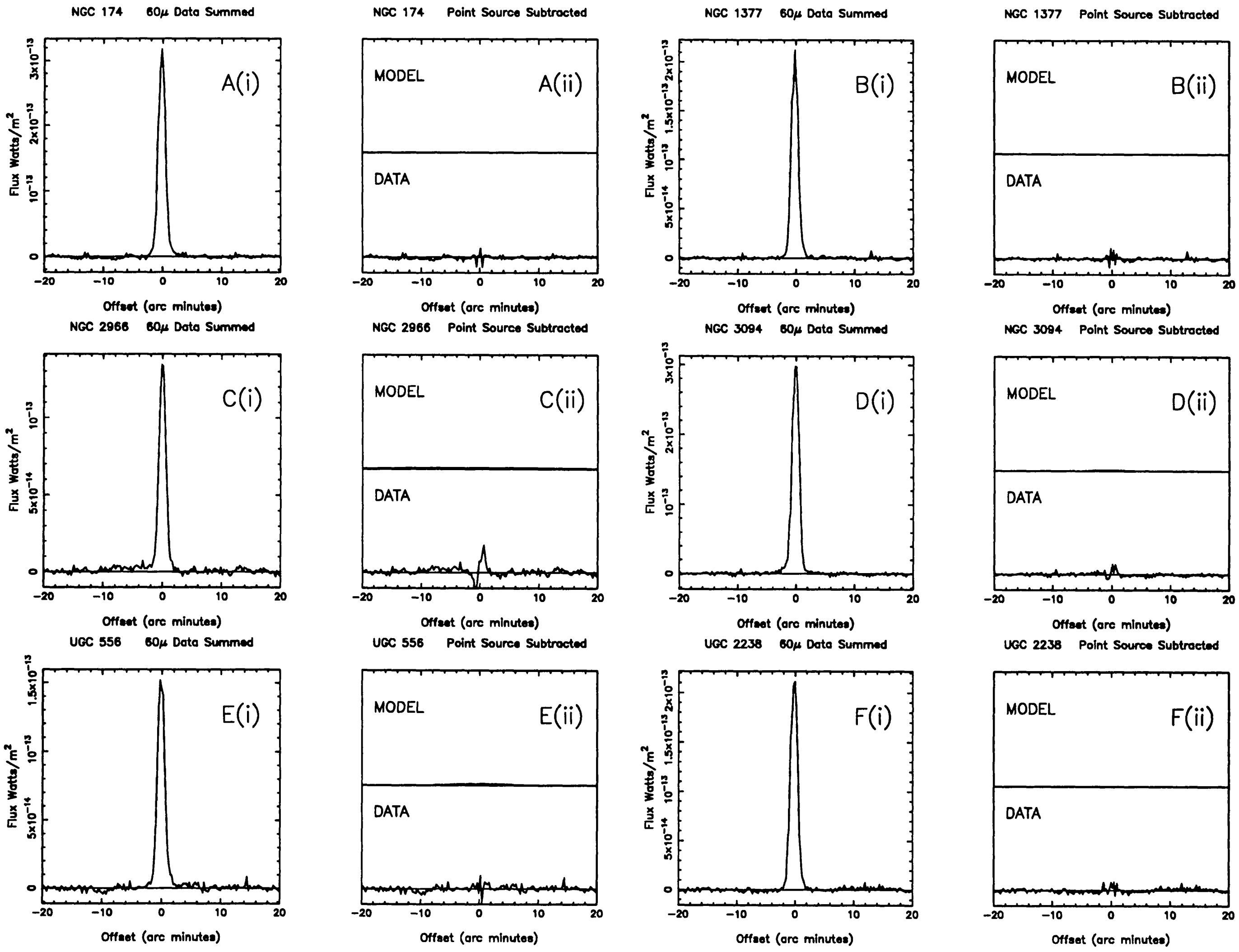

FIG. 16.—This figure shows plots of the same type as in Fig. 3, for the galaxies which were believed to be unresolved. As the upper portion of the (ii) plots show, the MFP did not fit a significant extended component to any of these test objects.

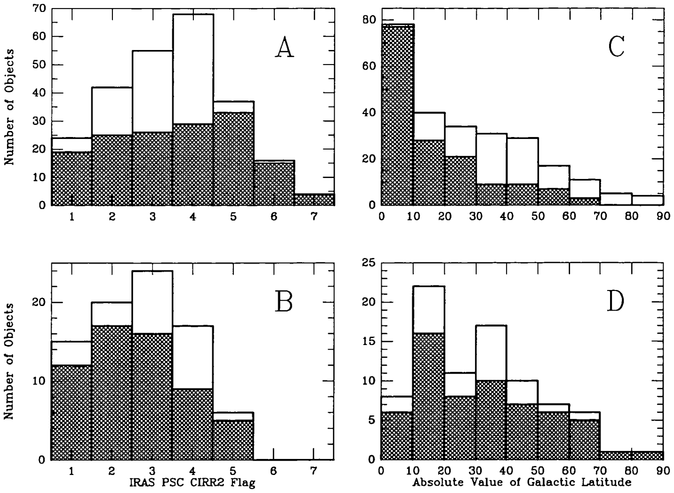

FIG. 17.—(a and b) The distributions of the PSC CIRR2 flag for the resolved and unresolved objects, respectively. We judged 248 objects to be unresolved; however, only 246 of these appear in the PSC (two failed to meet the strict confirmation criteria, even though individual *IRAS* observations show a strong detection). One resolved object, Y Hya, does not appear in the PSC and hence has no CIRR2 flag. (c and d) The distribution of Galactic latitudes among the unresolved and resolved objects. These two plots contain the objects which do not appear in the PSC. In all four plots the data from the CO selected sample are presented in the shaded regions.

extended emission reported by the MFP was caused by infrared cirrus.

Figures 17c and 17d show the distribution of absolute Galactic latitudes, $|b^{\rm II}|$, for the unresolved and resolved groups, respectively. The unresolved objects are clustered nearer to the Galactic plane than are the resolved ones, as one would expect if the resolved objects are less distant. The average $|b^{\rm II}|$ value of the resolved group is 31°.3. If the resolved objects were distributed randomly about the sky, $|b^{\rm II}|$ would average to 32°.7. This close agreement suggests that the average distance to the resolved objects is less than 1 kpc, the half thickness of the Galactic disk. The greater clustering of the unresolved objects about the Galactic plane explains the higher average CIRR2 value for that group.

As a final test, a function was defined to discriminate between cases where the MFP found significant amounts of extended emission, and those where it did not. The "quality function" is defined as

$$\mathrm{QF} = \frac{Q_0 F_{\rm ext}}{F_{\rm unres} R_{\rm out}^2}$$

where $F_{\rm ext}$ is the flux the model predicts from beyond 1′ from the point source, $F_{\rm unres}$ is the flux the model predicts from within 1′, $R_{\rm out}$ is the geometric mean of the dust shell's semimajor and semiminor axes, and Q_0 is the normalization constant. The ratio of the two fluxes in QF gives a measure of the fraction of the total flux arising from the resolved region of the CSS. The division by $R_{\rm out}^2$ is included to discriminate against model results predicting low intensity emission from a very large area, which is apt to be caused by slight curvature in the scan baselines. The QF function is normalized so that a spherical CSS with a radius of 5′ and $F_{\rm unres}/F_{\rm ext} = 10$ will have a QF value of 1. Values substantially less than 1 indicate the star is not resolved.

Figure 18 shows the values of QF for each star processed by the MFP, with a CIRR2 flag of 4 or less. In figure 18a, the QF values are displayed as a function of the distance to the source. Except for the case of R CrB, all of the large values of QF come from objects less than 1 kpc away. This implies that the extended emission found by the MFP arises from a real shell around a nearby object and is not a spurious feature of the data or the detector templates. Figure 18b shows the QF values as a function of 60 μm flux. Above average QF values were obtained for sources differing by more than a factor of 1000 in 60 μm flux, therefore the extended emission is not just an artifact caused by the templates matching either very weak or very strong sources poorly. Many of the objects in Figure 21b with 60 μm flux values below 10.0 Jy have large QF values. The average QF value for these 101 objects is 0.91. To check whether some defect in the MFP caused all faint objects to have high QF values, the data for 45 unresolved galaxies with flux values below 10 Jy were processed. The average QF for these galaxies was 0.18, which is less than the QF value for any of the objects we claim are resolved. Figure 18c shows the QF values as a function of the PSC VAR index, which is defined as 10 times the probability that a source is variable in the 12 or 25 μm bands. Above-average QF values are seen at all VAR index values, and the highest values are found for the stars which showed the least evidence of variability (there is, of course, no doubt that *all* of these objects, except the planetary nebulae, are long-period variables; the limited duration of the *IRAS* survey meant that most of them were only observed a few times, over a interval of less than one pulsation period). It therefore seems unlikely that intensity fluctuations caused by source variability confused the MFP and caused it to fit a spurious resolved component.

While these reliability tests give us confidence that most of the extended emission we have found is circumstellar in origin, we cannot be certain in any individual case that the emission is truly associated with the star. The extended emission found surrounding any of the Additional Objects should be regarded

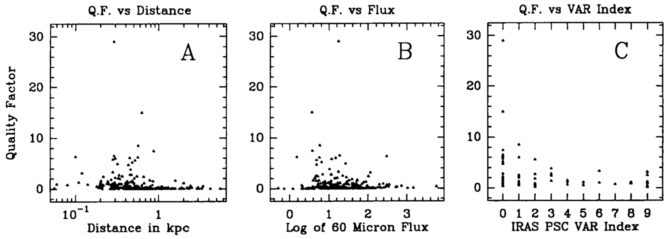

FIG. 18.—The distribution of "Quality Factor" values as a function of distance, 60 μm flux, and the *IRAS* PSC variability index. Higher values of QF correspond to sources that have been resolved. In (a–b), the QF is shown for all 263 stars which were processed by the MFP and which have CIRR2 values of 4 or less. The average QF value is 0.87, and many symbols overlap. Panel (a) does not include the stars IRAS 03074−8732, W Hor, T Com NSV 5868, NSV 1835, V2234 Sgr, NSV 12961, and IRAS 20541−6549, because no distance estimates were available for these stars. Z Cen is also not shown (see text). Forty-nine of the stars shown in (a) are at distances of 1 kpc or more. The star at 1.6 kpc with a QF greater than 1 is R CrB. Panel c, which includes only the 74 stars which were judged to be extended, shows the distribution of the PSC variability index among these objects.

TABLE 3

MODEL RESULTS FOR STARS FOUND TO BE EXTENDED

60μ Results

Name	R_{outer} (arcmin)	R_{inner} (arcmin)	F_{ps} (Jy)	F_{ext} (Jy)	Name	R_{outer} (arcmin)	R_{inner} (arcmin)	F_{ps} (Jy)	F_{ext} (Jy)
AQ And ^{B,H}	3.3	0.5	3.8	1.7	SW Vir	11.4	0.5	57.4	12.2
R Scl	6.5	1.1	60.4	6.1	R Hya	5.7	1.8	106.4	21.4
CRL 278	5.1	0.7	45.3	5.5	Z Cen ^{H,I}	6.7	2.1	33.5	3.1
o Cet ^{F}	2.2	0.0	287.0	89.1	W Hya	10.5	0.7	216.2	76.5
UX And ^{H}	3.6	0.7	13.3	1.3	θ Aps ^{H}	12.3	0.3	59.5	12.2
V Eri ^{A}	8.0	2.8	25.5	5.4	RX Boo	6.6	0.5	75.9	12.1
U Men ^{H}	13.6	3.9	27.5	3.6	RW Boo ^{H}	5.0	1.4	6.2	1.2
R Dor ^{H}	6.8	0.3	267.3	49.8	X TrA ^{C}	4.1	1.3	15.4	9.2
ST Cam	3.1	0.5	7.1	2.0	R CrB ^{H}	9.8	1.5	4.5	3.1
R Lep	4.8	0.4	28.8	2.7	ST Her ^{H}	5.7	0.9	18.8	2.9
W Ori	6.2	2.1	15.8	5.9	X Her	6.2	0.0	43.9	5.7
R Aur	4.0	0.1	24.7	5.7	S Dra ^{H}	7.7	2.0	13.6	1.5
R Oct ^{H}	10.1	5.3	7.8	5.6	V Pav ^{C,H}	3.8	1.3	11.3	3.7
W Pic	6.4	1.0	5.6	2.6	NGC 6720 ^{E}	5.4	0.1	55.1	13.7
α Ori ^{F}	10.5	0.2	302.9	165.2	δ^2 Lyr ^{H}	16.5	3.9	9.3	11.0
U Ori ^{C}	6.7	1.3	43.1	8.9	V Tel ^{H}	5.5	1.7	11.6	1.9
CRL 5185 ^{G,H}	10.4	0.5	578.1	148.5	V1942 Sgr ^{A}	3.2	0.2	2.7	3.2
UU Aur ^{C}	4.3	0.5	18.2	11.8	UX Dra ^{B}	4.0	0.2	5.0	2.1
IRC−10139 ^{H}	16.7	2.8	1.8	22.2	AQ Sgr ^{B}	3.0	1.2	6.0	3.4
NGC 2346	6.3	1.5	8.4	2.2	R Cyg	4.8	2.0	13.5	3.6
Y Lyn ^{C}	4.2	1.4	12.2	3.1	S Pav ^{H}	6.8	0.9	31.6	5.3
KK Car ^{H}	10.7	3.2	7.4	8.6	V1943 Sgr	5.0	0.9	29.7	7.7
X Cnc	8.9	1.2	7.6	1.2	X Pav	4.9	0.7	54.7	8.9
RS Cnc	5.8	1.0	36.7	4.0	RZ Sgr ^{C,H}	4.3	1.0	10.4	7.7
R Leo	3.8	0.8	127.0	29.0	RT Cap	8.1	1.0	5.1	3.1
IRC+10216 ^{D,F}	6.6	0.0	6048.3	441.9	T Mic ^{H}	5.6	0.6	34.6	7.7
Y Hya	9.7	1.3	8.3	3.6	T Ind	2.9	0.8	5.1	0.6
CIT 6 ^{F}	7.0	0.4	300.4	13.8	Y Pav ^{B}	5.8	0.6	7.2	3.0
U Ant ^{A}	4.7	0.6	28.6	15.4	S Cep	3.9	0.9	32.2	3.2
U Hya ^{A}	2.9	1.3	12.5	48.3	RV Cyg ^{A}	6.0	1.5	12.1	6.0
VY UMa ^{B}	3.1	0.1	4.4	1.7	EP Aqr	5.9	1.5	55.1	5.8
R Crt	5.9	1.9	59.5	9.2	PQ Cep ^{C}	7.3	2.1	10.1	2.6
IRC−30163E	6.8	2.3	33.9	7.1	W Peg ^{H}	7.3	3.4	14.3	2.6
RU Crt ^{H}	2.9	0.2	5.1	1.7	SV Peg	4.7	1.5	26.9	1.2
BK Vir	5.6	1.5	21.0	3.1	π^1 Gru	4.9	0.6	89.4	11.3
Y UMa	3.8	1.7	16.4	2.9	V PsA	5.1	1.2	19.8	2.4
Y CVn ^{B}	5.5	2.8	19.0	10.7	TX Psc	3.1	0.1	11.8	4.5
RY Dra	18.9	1.9	8.8	6.9	RS And ^{H}	19.3	3.5	10.4	5.1
RT Vir	4.1	1.0	40.7	6.3	R Cas ^{C}	4.3	1.0	116.5	27.0

100μ Results

Name	R_{outer} (arcmin)	R_{inner} (arcmin)	F_{ps} (Jy)	F_{ext} (Jy)	Name	R_{outer} (arcmin)	R_{inner} (arcmin)	F_{ps} (Jy)	F_{ext} (Jy)
V Eri ^{A}	8.9	1.0	5.6	7.5	RY Dra	22.1	5.3	4.4	31.1
U Men	18.7	7.3	7.8	13.2	SW Vir	15.0	4.7	15.4	23.5
R Dor	18.0	3.8	84.0	39.5	W Hya	15.0	2.4	72.0	65.1
W Pic	18.4	4.1	3.6	23.8	θ Aps	11.7	4.8	16.8	20.3
CRL 5185	16.7	0.2	414.9	462.1	RX Boo	12.6	4.8	25.1	16.6
KK Car	15.5	2.7	2.5	59.9	R CrB	13.0	1.0	1.2	9.1
IRC+10216	9.5	0.7	865.8	256.0	δ^2 Lyr	16.9	6.8	2.7	28.1
Y CVn ^{B}	6.3	1.2	5.9	11.0					

[A] These objects are listed as extended at 60 and 100 μm in the SSSC.

[B] These objects are listed as extended at 60 μm in the SSSC.

[C] These objects are listed as extended at 100 μm in the SSSC.

[D] IRC + 10°216 saturated the 60 μm detector and produced strong optical cross talk in the 60 μm band. The windows used to fit a baseline before processing were not free of these effects, and the 60 μm results given by the MFP are probably spurious. The 100 μm data are largely free of these effects.

[E] NGC 6720 is listed as extended at 12 and 25 μm in the SSSC.

[F] These values were obtained from fits to the small data set provided by the default ADDSCAN search radius of 1'.7. The data obtained using 10' search radius were not used, because they showed signs of optical cross-talk.

[G] CRL 5185 is listed as extended at all four *IRAS* bands in the SSSC. It is associated with the H II region S 270. The extended emission is apt to be associated with the surrounding molecular cloud.

[H] These stars are from the Additional Objects list.

[I] Z Cen is a Type I supernova which erupted in NGC 5253 during 1895. It is likely that the extended emission seen is due to the galaxy it is embedded in, rather than a circumstellar shell.

1993ApJS...86..517Y

with particular skepticism. A case in point is Z Cen, which the MFP found to be extended. This object is a Type I supernova in a nearby galaxy. It is very unlikely that the extended emission is related to the supernova, and even the association of the unresolved emission with the supernova is questionable.

4.1. 60 *Micron Results*

Table 3 shows the model parameters for the 78 stars found to be extended in the 60 μm data. While all stars with QF > 1.5 are included in this table, stars with QF $\approx$ 1 were included only if the extended model appeared to fit the CRDD data appreciably better than a point source did. The fluxes quoted are not color corrected and were converted from the raw units of W m^{-2} to Janskys by assuming a flat energy spectrum $\nu F_\nu = 1$. The radii given in Table 3 are the geometric means of the major and minor axes of the best-fit ellipsoidal shell.

4.2. 100 *Micron Results*

At first glance, the 100 μm data would seem to hold the most promise for detecting extended emission. The cool outer regions of the CSS should radiate most strongly around 100 μm, even if the dust emissivity has a wavelength dependence as strong as λ^{-2}. In addition, the warm inner unresolved region will be relatively less dominant at 100 μm than at 60 μm. Unfortunately, there are problems with the 100 μm survey data that more than offset these advantages.

By far the worst problem with the 100 μm data is the contamination of much of the sky by infrared cirrus. When the 100 μm data for the 78 stars which were resolved in the 60 μm data were examined, most of the scans were strongly curved, presumably due to infrared cirrus. In these cases even when the individual scans showed extended emission surrounding the star, it was impossible to find regions of the scan which were clearly free of emission that could be used to calculate the scan's baseline. The results of the MFP depend very strongly on the position of the scans' baselines, therefore if no baselines could be calculated, the scans could not be used. Only 16 of these 78 stars are in regions so free of cirrus emission that baselines could be calculated and the 100 μm data could be processed with the MFP. In all cases except RY Dra, all scans passing within 10′ of the star's position were analysed. For RY Dra, all scans passing within 25′ were used.

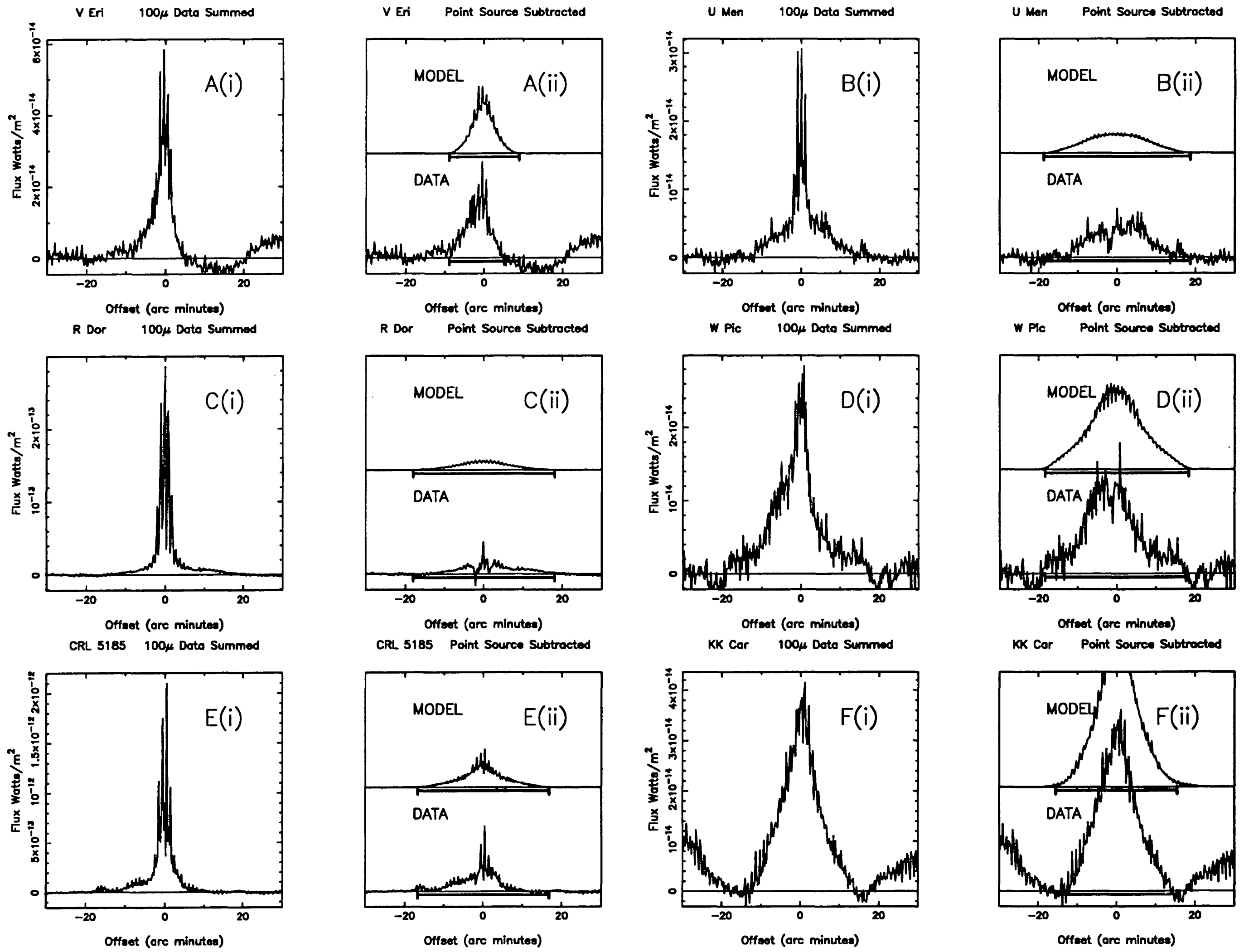

FIG. 19.—This figure shows plots of the same type as in Fig. 3, using the 100 μm CRDD data for the stars V Eri, U Men, R Dor, W Pic, CRL 5185 and KK Car. The bins used in these plots were 0.′50 wide, twice the size used in Figs. 4–17.

As an initial test, 100 μm data for several unresolved galaxies were processed with the MFP. The MFP found almost all of them to be slightly resolved. This indicated that the 100 μm detector response functions did not fit the survey data as well as the 60 μm functions did. The cause of this is apt to be the fact that the 100 μm data stream was passed through a 1.5 Hz low-pass filter (the filter for the 60 μm data rolled off at 3 Hz). At the survey scan rate of $3'.85\ \mathrm{s}^{-1}$, this severe filtering significantly broadened the response to a point source beyond the $44''$ diffraction limit. The response functions were derived from pointed observations taken at $\frac{1}{2}$ the survey scan rate, and therefore did not suffer as great a broadening. In order to compensate for this mismatch, the 100 μm response functions were stretched in the in-scan direction until the MFP reported that the test galaxies were unresolved. The required stretch factor was 16%. Even after the response functions had been modified in this way, comparison of the CRDD data with simulated data produced with the response functions showed that the 100 μm response functions did not fit the data as well as the 60 μm functions did. For this reason only the stars with dramatically extended CSSs or very high signal/noise will be considered to have been resolved in the 100 μm data. These stars are listed in Table 3, and the MFP results are shown in Figures 19–21.

All the stars found to be resolved in the 100 μm band show a larger shell in the 100 μm data than in the 60 μm data, though in some cases the difference is quite small. Since the model derived by the MFP is convolved with the detector response functions before it is compared with the data, the larger 100 μm size is not an artifact of the telescope's poorer resolution at 100 μm. It is likely that the size difference arises from a radial temperature gradient in the envelope. A similar systematic difference in the 60 and 100 μm sizes was found by Hawkins & Zuckerman (1991), who deconvolved the *IRAS* data for the strongest infrared planetary nebulae. Three of the objects resolved in both 60 and 100 μm appear at least 50% larger in the 100 μm data (W Pic, W Hya, and RX Boo). It is likely that for these objects, the outer extent of the model 60 μm shell only reflects the point at which emission falls below the detectors' noise level, rather than the true extent of the shell. Because these three objects represent almost half of the objects for which we have good data in both FIR bands, we suspect that many of the 60 μm outer radii for the other stars listed in Table 3 also are smaller than the full extent of the CSSs.

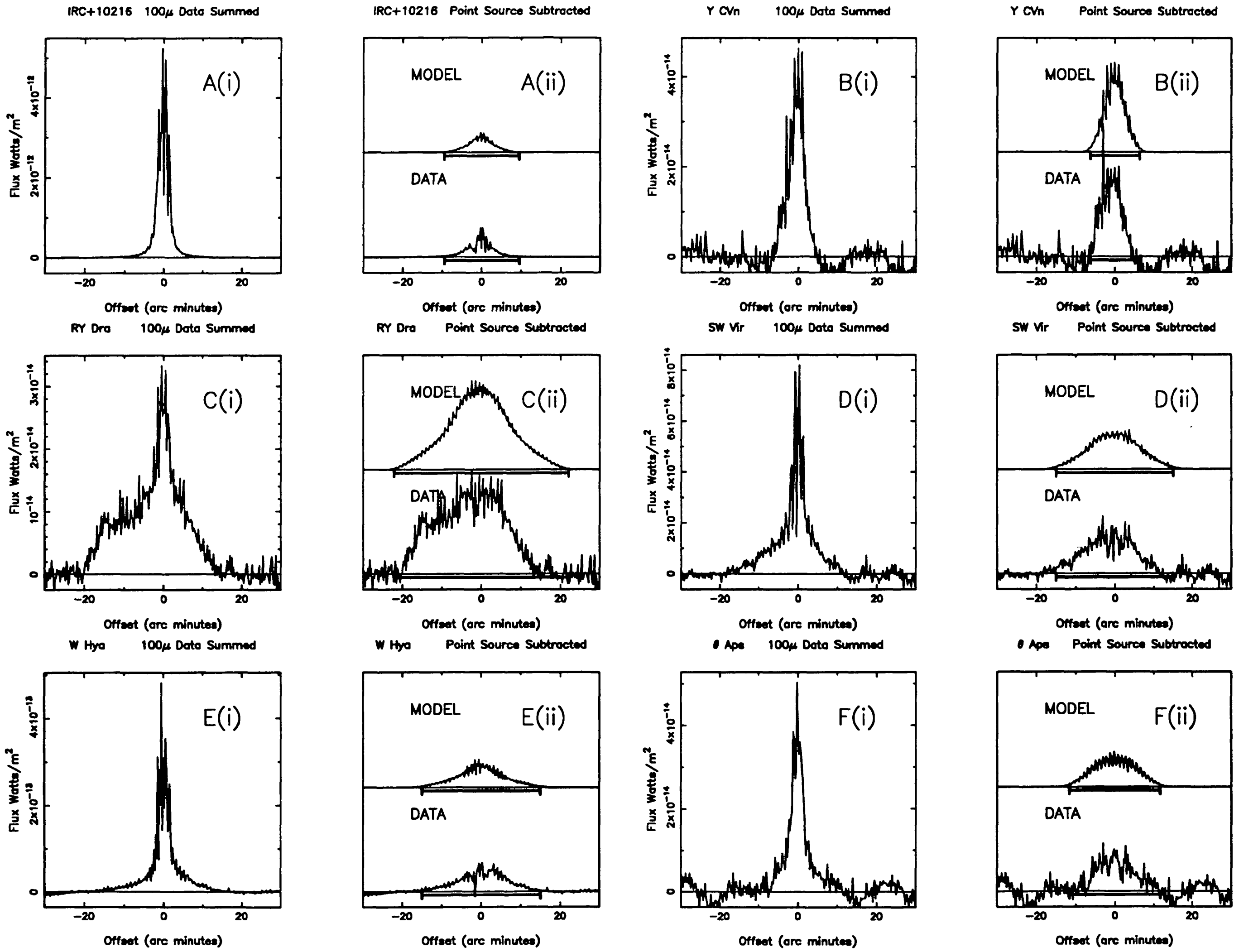

FIG. 20.—This figure shows plots of the same type as in Fig. 19, for the stars IRC +10216, Y CVn, RY Dra, SW Vir, W Hya, and θ Aps

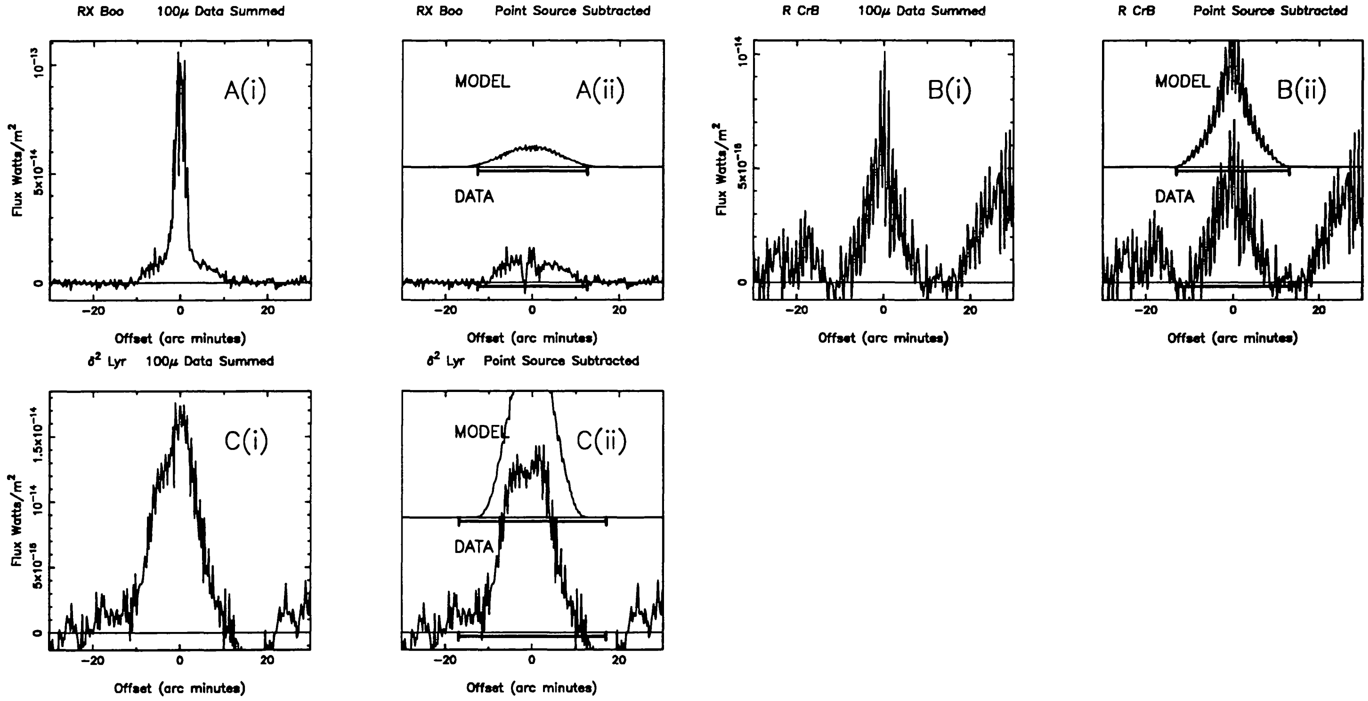

FIG. 21.—This figure shows plots of the same type as in Fig. 19, for the stars RX Boo, R CrB, and δ^2 Lyr

5. CONCLUSIONS

Seventy-eight of the 512 stars we examined appear to be extended in the *IRAS* 60 μ survey data. In the case of 2 of these stars, Z Cen and CRL 5185, the extended emission is not apt to have arisen in a circumstellar shell. Due to cirrus contamination and problems with our understanding of the characteristics of the *IRAS* detectors, there are only 15 of these stars for which the evidence of extended emission at 100 μm is convincing.

We would like to thank the staff of IPAC for their help; particularly Linda Fulmer and Mehrdad Moshir, for patiently describing the *IRAS* data; Helen Hanson, Rosanne Hernandez, and Hilary Hope, who cheerfully and quickly processed dozens of requests for CRDD data and Joe Mazzarella for help using IPAC's CATSCAN data base system, which was used to select the stars on the Additional List. This work was supported by NASA contract NAG 5-1153 and NSF contract No. AST 90-15755.

REFERENCES

Bauer, W. H., & Stencel, R. E. 1992, in Proc. 7th Cambridge Workshop on Cool Stars, Stellar Systems, and the Sun ASP Conf. Ser., Vol 26 (San Francisco: ASP), 478
Bowers, P. F., & Hagen, W. 1984, ApJ, 285, 637
Gillet, F. C., Backman, D. E., Beichman, C., & Neugebauer, G. 1986, ApJ, 310, 842
Hawkins, G. W. 1989, BAAS, 21, 1112
———. 1990, A&A, 229, L5
Hawkins, G. W., & Zuckerman, B. 1991, ApJ, 374, 227
IRAS Point Source Catalog. 1985, Joint *IRAS* Science Working Group (Washington, DC: US GPO)
IRAS Small-Scale Structure Catalog. 1985, Joint *IRAS* Working Group (Washington, DC: US GPO)
Jura, M., & Kleinmann, S. G. 1992, ApJS, 79, 105
Moshir, M., et al. 1989, Explanatory Supplement to the *IRAS* Faint Source Survey preprint
Olnon, F. M., Raimond, E., & *IRAS* Science Team. 1986, A&AS, 65,607
Press, W. H., Flannery, B. P., Teukolsky, S. A., & Vetterling, W. A. 1986, Numerical Recipes (Cambridge Univ. Press)
Soifer, B. T. 1989, private communication
Stencel, R. E., Pesce, J. E., & Bauer, W. H. 1988, AJ, 95, 141
———. 1989, AJ, 97, 1120